

Mapping the Asymmetric Thick Disk: III. The Kinematics and Interaction with the Galactic Bar¹

Roberta M. Humphreys^{2,3}, Timothy C. Beers⁴, Juan E. Cabanela^{5,3}, Skyler Grammer²,
Kris Davidson², Young Sun Lee⁴, Jeffrey A. Larsen^{6,3}

roberta@umn.edu, beers@pa.msu.edu, cabanela@mnstate.edu,
grammer@astro.umn.edu, kd@astro.umn.edu, lee@pa.msu.edu, larsen@usna.edu

Received _____; accepted _____

To appear in the *Astronomical Journal*

¹Based on observations obtained at the MMT Observatory, a joint facility of the Smithsonian Institution and the University of Arizona and at the Cerro Tololo Interamerican Observatory (NOAO) operated by the Association of Universities for Research in Astronomy (AURA).

²Astronomy Department, University of Minnesota, Minneapolis, MN 55455

³Visiting Astronomer, Cerro Tololo Interamerican Observatory (CTIO), National Optical Astronomy Observatory (NOAO), which is operated by the Association of Universities for Research in Astronomy (AURA), Inc., under cooperative agreement with the National Science Foundation (NSF).

⁴Department of Physics and Astronomy and the Joint Institute for Nuclear Astrophysics,, Michigan State University, East Lansing, MI 48824

⁵Department of Physics and Astronomy, Minnesota State University Moorhead, Moorhead MN, 56563

⁶Physics Department, United States Naval Academy, Annapolis, MD 21402

ABSTRACT

In the first two papers of this series, Larsen et al (2010a,b) describe our faint CCD survey in the inner Galaxy and map the over-density of Thick Disk stars in Quadrant I (Q1) to 5 kpc or more along the line of sight. The regions showing the strongest excess are above the density contours of the bar in the Galactic disk. In this third paper on the asymmetric Thick Disk, we report on radial velocities and derived metallicity parameters for over 4000 stars in Q1, above and below the plane and in Q4 above the plane. We confirm the corresponding kinematic asymmetry first reported by Parker et al. (2004), extended to greater distances and with more spatial coverage. The Thick Disk stars in Q1 have a rotational lag of $60 - 70 \text{ km s}^{-1}$ relative to circular rotation, and the Metal-Weak Thick Disk stars have an even greater lag of 100 km s^{-1} . Both lag their corresponding populations in Q4 by $\approx 30 \text{ km s}^{-1}$. Interestingly, the Disk stars in Q1 also appear to participate in the rotational lag by about 30 km s^{-1} . The enhanced rotational lag for the Thick Disk in Q1 extends to 4 kpc or more from the Sun. At 3 to 4 kpc, our sight lines extend above the density contours on the near side of the bar, and as our lines of sight pass directly over the bar the rotational lag appears to decrease. This is consistent with a “gravitational wake” induced by the rotating bar in the Disk which would trap and pile up stars behind it. We conclude that a dynamical interaction with the stellar bar is the most probable explanation for the observed kinematic and spatial asymmetries.

Subject headings: Galaxy: structure, Galaxy: kinematics and dynamics

1. Introduction: The Asymmetric Thick Disk

An excess of faint blue stars in Quadrant 1 (Q1) of the Galaxy compared to complementary fields in Quadrant 4 (Q4) was initially recognized by Larsen & Humphreys (1996). Parker et al. (2003) subsequently extended the survey to a much larger contiguous region covering several hundred square degrees. They confirmed the original findings, mapped the stellar excess in Q1 from $l \sim 20 - 55^\circ$ and $b \sim 20 - 45^\circ$, and argued for a comparable asymmetry in Q1 below the plane. The stars showing the excess were probable Thick Disk stars, 1 - 2 kpc from the Sun. Parker et al. (2004) also reported an associated kinematic signature. Velocities and metallicities of stars in 12 fields in Q1 and Q4 showed that the Thick Disk stars in Q1 have a much slower effective rotation rate ω , compared to the corresponding Q4 stars, with a significant lag of 80 to 90 km s^{-1} in the direction of Galactic rotation, greater than the expected lag of 30 to 50 km s^{-1} (Reid 1998; Chiba & Beers 2000; Carollo et al. 2010) for the canonical Thick Disk population.

Interpretation of the asymmetry, now referred to as the Hercules Thick Disk Cloud (Larsen et al. 2008), is not straightforward. It is tempting to assume that the asymmetry is the fossil remnant of a merger, however the star counts were also consistent with a triaxial Thick Disk or Inner Halo, with its axis in Q1, as well as with a gravitational interaction with the stellar bar in the disk (Weinberg 1992; Hammersley et al. 2000). The latter is especially intriguing given the corresponding asymmetry in the kinematics. A triaxial Thick Disk could also yield different effective rotation rates because of noncircular streaming motions along its major axis. The star count excess appears to terminate near $l \sim 55^\circ$ (Parker et al. 2003). To search for evidence of triaxiality, in Paper I (Larsen et al. 2010a) we extended the star counts to fainter magnitudes, corresponding to greater distances, from l of 50° to 75° . The fields at 55° to 75° , show no significant excess, including the faintest magnitude interval, and therefore, do not support a triaxial interpretation of the asymmetry.

The outstanding question relevant to the origin of the Hercules Cloud is its spatial extent along the line of sight and its associated kinematics. In Papers I and II (Larsen et al. 2010b) in this series we describe our faint CCD survey to map the spatial extent of the over-density. The photometric survey covers 47.5 square degrees in 63 fields in Q1 and Q4 above and below the Galactic plane. Except for fields with $b \sim 30 - 40^\circ$ in Q1, most of these regions are not covered by the Sloan Digital Sky Survey (SDSS, York et al. (2000)). Larsen et al. (2010b) find that the over-density or star count asymmetry in Q1 extends to approximately 5 kpc along our line of sight, and that the regions showing the excess interestingly are above the near side of the density contours for the bar in the Disk (Weinberg 1992). We have also extended our corresponding spectroscopic survey to fainter magnitudes and greater spatial coverage. We have obtained additional medium-resolution spectra and now have radial velocities and metallicity estimates for more than 4000 stars in 31 fields. In the next section we describe the observations and data reduction. In §3 we discuss the kinematics and confirm the asymmetry between the stars in Q1 and Q4, and in §4 we use the metallicity information from the spectra to separate the stars into the different populations. We determine the rotational lag for the different populations in §5, and in the concluding section we summarize the kinematic and spatial asymmetries in the Hercules Cloud and its interaction with the Galactic bar in the Disk.

2. Observations and Data Reduction

One of the goals of the spectroscopy program is to obtain more complete spatial coverage and extend the survey to greater distances than were available to Parker et al. (2004). In addition to their original 12 fields, we added 13 fields in Q1 above and below the plane and 6 fields in Q4 above the plane. The distribution of the fields on the sky is shown in Figure 1. The stars were randomly chosen from our photometric catalogs

to have a wide range in apparent magnitude. Most of the targets were selected to have extinction-corrected $B - V$ colors ≤ 0.6 mag. This color cut was adopted to isolate a population dominated by Thick Disk and Halo stars. In the case of those fields selected from the MAPS Catalog of the POSS I (Cabanela et al. 2003)¹, we used an $O - E$ color of ≤ 1.0 mag, corrected for interstellar extinction, which corresponds to $B - V \approx 0.6$ mag.

The spectra were obtained with the Hectospec Multi-Object Spectrograph (MOS) (Fabricant et al 1998) on the MMT 6.5m telescope on Mt. Hopkins for the northern fields in 2007 and 2008 and with the Hydra MOS on the Blanco 4m at CTIO in 2006 and 2008 for the fields with declinations below -20° . The stars selected for observation with the Hectospec range in V magnitude from 16 to 19 mag and for Hydra from 15 to 18 mag; 1 to 2 magnitudes fainter than used in Parker et al. (2004); consequently, the total exposure times were long to get adequate S/N for the faintest stars, ~ 10 , for reliable velocities. A summary of the observations is provided in Table 1.

The Hectospec² has a 1° FOV and uses 300 fibers each with a core diameter of $250\mu\text{m}$ subtending $1''.5$ on the sky. We used the 600 l/mm grating with the 4800\AA tilt yielding $\approx 2500\text{\AA}$ coverage with $0.54\text{\AA}/\text{pixel}$ resolution and R of ~ 1700 . The Hydra MOS³ has 138 $2''$ fibers with a $40'$ FOV. We used it with the SiTe 2K x 4K CCD detector and the KPGL1 632 l/mm grating plus BG39 filter with the grating tilted for 4167\AA yielding $0.58\text{\AA}/\text{pixel}$ resolution, $R \sim 1100$, and $\approx 2400\text{\AA}$ coverage. In 2006 we observed additional stars in several of the fields included in Parker et al. (2004) to increase the number of stars in some of the southern fields for comparison with their corresponding fields in the north. These settings are thus the same that they used, but with a new CCD detector.

¹<http://aps.umn.edu>

²<http://www.cfa.harvard.edu/mmti/hectospec.html>

³<http://www.ctio.noao.edu/spectrographs/hydra/hydra.html>

The Hectospec data was reduced using ESPECROAD⁴, a portable version of the CfA/SAO data reduction pipeline. Hydra has its own data reduction package within the Image Reduction and Analysis Facility software package (IRAF⁵). Both software packages have multiple tasks for flat fielding, fiber throughput correction, wavelength calibration, spectrum extraction, and sky subtraction. The separate exposures, often obtained on different nights, were coadded and cosmic rays removed. The radial velocities were measured with the IRAF task RVIDLINES. We manually identified 2 to 3 spectral lines and then relied on RVIDLINES to automatically identify the remaining lines from a list we created including the Balmer series, the Ca II H and K lines, and strong metallic lines found in A-G-type dwarf stars. We selected lines that could be clearly distinguished from the noise. Misidentified lines were rejected based on large velocity residuals. For the majority of the stars the velocity error is better than $\sigma_{helio} \sim 5 \text{ km s}^{-1}$. Standard stars were also observed each night, and in all cases their measured velocities agree well with the published velocities.

Together with the 741 radial velocities from Parker et al. (2004), we now have velocities for 4151 stars, 1814 and 1210 in Q1, above and below the plane, respectively, and 1127 in Q4. A supplemental catalog is available on-line with all of the velocity data plus the metallicity and atmospheric parameters described below. Tables A1 and A2 are described in the Appendix with sample data.

⁴Developed by Cabanela in consultation with Doug Mink and other staff at CfA and available with documentation for download at <http://iparrizar.mnstate.edu/juan/research/ESPECROAD>

⁵IRAF is written and supported by the IRAF programming group at the National Optical Astronomy Observatories (NOAO) in Tucson, Arizona. NOAO is operated by the Association of Universities for Research in Astronomy (AURA), Inc. under cooperative agreement with the National Science Foundation

Figures 2 and 3 show histograms of the V magnitudes and $B-V$ colors for the stars with velocities in Q1 and Q4. The colors are corrected for interstellar extinction using the maps from Schlegel et al. (1998). There are fewer stars with velocities at the faintest magnitudes in Q4 because they were all obtained with Hydra. The color histograms demonstrate that similar populations of stars were selected for velocities in the three regions.

We have determined metallicity estimates and atmospheric parameters based on procedures similar to those used for stars in the Sloan Digital Sky Survey (SDSS: York et al. 2000; Abazajian et al. 2009). We applied a newly developed version of the SEGUE Stellar Parameter Pipeline (SSPP: Lee et al. 2008a,b; Allende Prieto et al. 2008), called the n-SSPP⁶ suitable for application to medium-resolution spectra other than those taken by SDSS/SEGUE. The n-SSPP uses the Johnson V magnitude and $B - V$ color, and/or a 2MASS (Cutri et al. 2003) J magnitude and $J - K$ color, corrected for a interstellar absorption and reddening, together with an estimate of the observed radial velocity. The program determines estimates of the primary atmospheric parameters (T_{eff} , $\log g$, $[Fe/H]$, $[\alpha/Fe]$) and their errors, as well as estimates of distance, making use of a subset of the procedures described in Lee et al. (2008a, 2010). Note that it is not necessary that the input spectra be flux calibrated, or continuum rectified. It is also not strictly necessary to supply input colors, since the n-SSPP makes internal estimates that can be used as needed, but due to possible degeneracies in the derived parameters color information is certainly preferred.

We used the n-SSPP to obtain metallicity and atmospheric parameter estimates for all of our program stars with acceptable spectra, including the data from Parker et al. (2004), which were reprocessed with the new pipeline so that all of the parameters are on the same system. Rejected spectra include those with too low S/N ratios, or other problematic

⁶The non-SEGUE Stellar Parameter Pipeline

behavior. The input $B - V$ colors are from our own CCD measurements, or estimated from the MAPS $O - E$ colors. The J magnitudes $J - K$ colors are from the 2MASS Point Source Catalog, absorption corrected or de-reddened according to the Schlegel et al. (1998) dust maps. The derived parameters include the metallicity measurements, $[\text{Fe}/\text{H}]$ and $[\alpha/\text{Fe}]$, and the atmospheric parameters T_{eff} and $\log g$. The errors in the derived parameters by the n-SSPP are very similar to those that the SSPP claims. The typical errors of the SSPP are 141 K, 0.23 dex, and 0.23 dex for T_{eff} , $\log g$, and $[\text{Fe}/\text{H}]$, respectively, after combining small systematic offsets quadratically for stars with $4500 \text{ K} \leq T_{\text{eff}} \leq 7500 \text{ K}$ (Lee et al. 2008a). The distance from the Sun is derived from the photometry and the atmospheric parameters and are accurate to 10% to 20% (Beers et al. 2000). The input quantities and derived parameters with their errors are included in Tables A1 and A2 described in the Appendix. Figures 4 and 5 show the histograms for T_{eff} and $\log g$ from the n-SSPP pipeline. There are approximately the same relative numbers of stars over the range of temperatures in each region. The few relatively warm stars, $T_{\text{eff}} > 7000\text{K}$, are most likely horizontal branch stars in the Halo. The similar $\log g$ distributions also indicate that the greater majority of stars in our sample are main sequence.

3. The Kinematics

Figures 6 and 7 show the normalized histograms of the measured velocities corrected to the Local Standard of Rest (V_{LSR}) and the angular velocity of rotation ω for Q1 above and below the plane and for Q4 above the plane. The heliocentric velocities were corrected to the LSR using the solar motion ($u_{\odot} = 9\text{kms}^{-1}$, $v_{\odot} = 12\text{kms}^{-1}$, $w_{\odot} = 7\text{kms}^{-1}$) reported in Ibata et al. (1997) from *Hipparcos* data. ω was calculated using the standard equation with $R_{\odot} = 8 \text{ kpc}$ (Reid 1998), $V_{\odot} = 220 \text{ km s}^{-1}$, and $\omega_{\odot} = 27.5 \text{ km s}^{-1} \text{ kpc}^{-1}$. Both quadrants show a wide range of velocities with high velocity tails extending to negative velocities in

Q1 and to positive velocities in Q4. These high velocity tails are due to a non-rotating or slightly retrograde Halo relative to the LSR, and are expected to be negative in the direction of Galactic rotation in Q1 and positive in Q4. Due to the addition of fainter stars in our observations, we find a larger number of very high velocity Halo stars in both quadrants than Parker et al. (2003), including a few with $V_{LSR} \geq \pm 400 \text{ km s}^{-1}$.

The mean LSR velocities and ω for each direction are in Table 2, excluding the obviously high velocity stars with V_{LSR} greater than $\pm 200 \text{ km s}^{-1}$. The velocity distributions in Q1 above (Q1A) and below (Q1B) the plane are very similar with essentially the same mean V_{LSR} and ω , while the kinematic asymmetry between Q1 and Q4 is quite apparent. Assuming an axisymmetric Thick Disk that is rotating about the Galactic center, we would expect to measure positive LSR velocities in Q1, as these stars are moving away from us, and negative velocities in Q4 since the stars would be approaching. The velocities should be comparable for stars at similar distances and symmetric directions but of opposite sign. At typical distances from the Sun, of 2 to 3 kpc, corresponding to the mean V magnitudes, 17 to 18 mag, and assuming that most of these stars are near the main sequence turnoff, the expected V_{LSR} velocities in Q1, for example, should be $\approx 10\text{--}27 \text{ km s}^{-1}$. However, the Thick Disk is known to rotate slower or lag the Disk by up to 50 km s^{-1} . The observed LSR velocities for the Thick Disk would be expected to show a relative net shift with respect to the Disk velocities in both quadrants, to more negative velocities in Q1 and to more positive velocities in Q4. The stars in Q1 have a significant mean shift of 45 km s^{-1} up to 65 km s^{-1} while Q4 stars have a smaller shift and a mean V_{LSR} more consistent with the expected velocities. The much greater shift in Q1 with respect to the expected velocities shows a clear asymmetry between the two directions.

The results for the angular velocity of rotation, ω , between the two quadrants illustrates the greater net lag with respect to Galactic rotation in Q1. In these directions,

in the inner Galaxy ($l = 20\text{--}50^\circ$) most of the stars will be at distances from the Galactic center that range from 6 to 7.5 kpc. Using the power-law fit to the rotation curve in Brand & Blitz (1993), stars at these Galactocentric distances would have an expected ω of 30 to 39 $\text{km s}^{-1} \text{kpc}^{-1}$. The mean ω for Q4, $31.3 \pm 0.6 \text{ km s}^{-1} \text{kpc}^{-1}$, is thus marginally consistent with Galactic rotation with perhaps only a small lag. The stars in Q1, however, have a much slower effective rotation, with a mean ω of only $19.6 \pm 0.5 \text{ km s}^{-1} \text{kpc}^{-1}$, thus confirming the kinematic asymmetry between Q1 and Q4.

The velocities for the individual fields are in Appendix B. Four of the fields in Q1 are paired directly across the Galactic plane ($b = 0^\circ$), and nine fields in Q4 have complementary fields in Q1 across the $l = 0^\circ$ line. In all four cases in Q1, the mean V_{LSR} velocities and rotation rates agree to well within the standard error while the matching fields in Q1A and Q4 exhibit the slower rotation and greater lag in Q1. The three fields, H050+31, H050-31, and H310+31, illustrate the differences quite well. H050+31 and H050-31 have remarkably similar mean V_{LSR} 's and ω 's of $\sim -51 \text{ km s}^{-1}$ and 17 to 18 $\text{km s}^{-1} \text{kpc}^{-1}$, while the field at the same latitude and complementary longitude, H310+31, has a mean V_{LSR} of $+8.7 \text{ km s}^{-1}$ and mean ω of 26 $\text{km s}^{-1} \text{kpc}^{-1}$. All three fields show slower effective rotation rates and a lag with respect to Galactic rotation, but it is much greater in Q1. They illustrate the kinematic symmetry in Q1 and asymmetry between Q1 and Q4.

The SDSS Data Release 7 overlaps our higher latitude fields in Q1 at $b \sim 30\text{--}40^\circ$. As a check on our results, we queried the SDSS database from $b = 30\text{--}40^\circ$ and $l = 20\text{--}50^\circ$. We transformed the SDSS magnitudes and colors to Johnson V and B-V (Jordi et al. 2006), corrected them for interstellar extinction, and corrected the velocities to the LSR. Adopting our magnitude, color and V_{LSR} ranges, the mean V_{LSR} for 1747 stars in this region is $-37.8 \pm 1.9 \text{ km s}^{-1}$ with a mean ω of $16.9 \pm 0.6 \text{ km s}^{-1} \text{kpc}^{-1}$, comparable to our results in Q1 for fields at similar latitudes. This result not only confirms our results with

independent data, but also demonstrates that the rotational lag and presumed asymmetry extends across a large contiguous region in l and b .

One of the fields in Q1 below the plane, H048-45, has an anomalously negative velocity distribution and a large negative mean V_{LSR} compared with the other fields in Q1. The other characteristics of the stellar population, metallicities, colors, and magnitude distribution, appear to be normal. The origin of its very negative velocity distribution is not known. It is not included in the subsequent analysis, but is discussed separately later.

The velocities and rotation rates discussed in this section represent a mixture of Disk, Thick Disk, and Halo stars⁷. In the next section we use the additional information on their metallicities to examine their kinematics as a function of stellar population.

4. Metallicities and Population Separation

Figure 8 shows the normalized metallicity distribution functions (MDFs) in the three regions for all of the stars with $[Fe/H]$ derived from the n-SSPP pipeline described in §1. The predominance of low-metallicity stars in our sample confirms our color selection criteria. The three regions have very similar MDFs with mean $[Fe/H]$ of -1.14, -0.90, and -1.15 for Q1A, Q1B, and Q4, respectively. The mean error in $[Fe/H]$ is 0.05 *dex* over all the fields with a standard deviation of 0.04 *dex*. All three regions have a significant low metallicity tail. Removing the high velocity stars with $V_{LSR} \geq \pm 200 \text{ km s}^{-1}$ does not significantly alter the mean $[Fe/H]$ values. Q1B and Q4 have several objects with positive values for $[Fe/H]$. For many of the fields in these two regions, the stars for velocities were

⁷Some authors prefer old or thin disk. In this paper we simply use Disk to refer to this population. We also use Halo for what is likely a mix of Inner and Outer Halo stars in this paper.

initially selected from the MAPS Catalog before the CCD photometry was available. The more uncertain photographic colors may have led to more stars with redder B-V colors and therefore more Disk stars in the samples.

In our previous study (Parker et al. 2004) we removed the high velocity stars and simply used $[\text{Fe}/\text{H}]$ to separate the three primary populations, but recent studies of Disk and Thick Disk stars have demonstrated that $[\text{Fe}/\text{H}]$ alone is not sufficient to separate these two populations. Thick Disk stars primarily have $[\text{Fe}/\text{H}]$ between -0.5 and -1.2 (Wyse 2009) although, a mix of Disk and Thick Disk stars are now recognized with metallicities between 0 and -0.5 (Bensby, Feltzing & Lundstrom 2003; Nissen et al 2002). Furthermore, Chiba & Beers (2000) and Carollo et al. (2010) have argued for a Metal-Weak Thick Disk (MWTD) with somewhat lower metallicities, different kinematics, and a higher scale height than the canonical Thick Disk. This additional population ($-1.8 < [\text{Fe}/\text{H}] < -0.8$) overlaps the expected metallicity distributions of the Thick Disk and the Inner Halo. The primary goal of this study is to investigate potential differences in the kinematics of the populations between Q1 and Q4. We must apply the same selection criteria to all three regions. Consequently, we have chosen not to rely on their presumed kinematic properties, which we already know are different, to aid in the population separation. Instead we use the abundance parameters, $[\text{Fe}/\text{H}]$, $[\alpha/\text{Fe}]$, in combination with the stars' distances from the Galactic plane ($|Z|$), to separate the four populations: Disk, Thick Disk, MWTD, and Halo. Given the errors in the individual measurements for these parameters from our moderate-resolution spectra, plus the natural spread and overlap among these populations, we do not expect a clean separation, especially between Disk and Thick Disk, and Thick Disk and MWTD. The high-velocity stars are excluded from the population criteria described below.

The Disk. We initially assign to the Disk all stars with $[\text{Fe}/\text{H}] \geq 0$ and within 650 pc of

the Galactic plane, twice the expected scale height of the old or thin Disk population, and assume that this group represents a relatively uncontaminated Disk population. However, some Disk stars are also observed with $[\text{Fe}/\text{H}]$ values as low as -0.5 to -0.7 and thus overlap in metallicity with the Thick Disk population (Bensby, Feltzing & Lundstrom 2003, 2004; Nissen et al 2002). Due to their different enrichment histories from Type II and Type Ia supernovae, the ratio of the α -elements to Fe, in combination with the $[\text{Fe}/\text{H}]$ parameter, fortunately provides for a separation of Disk and Thick Disk stars with $[\text{Fe}/\text{H}]$ less than solar (see review by Feltzing & Bensby (2008)). The plots of $[\alpha/\text{Fe}]$ vs $[\text{Fe}/\text{H}]$ for the three regions in Figure 9 show the prominent bend or “knee” in the distribution at $[\text{Fe}/\text{H}] \approx -0.5$ observed by other authors. The sloping distribution from $[\text{Fe}/\text{H}] \approx 0$ to -0.5 , however, is a mix of Disk and Thick Disk stars. Since Disk stars typically have $[\alpha/\text{Fe}]$ values less than 0.2, and Thick Disk stars ≥ 0.3 , accurate abundances for the α -elements, derived from high-resolution spectra, permit the separation of the Disk and Thick Disk in this region. The mean error in $[\alpha/\text{Fe}]$ in our data is 0.04 with a standard deviation of 0.012. With the uncertainties in the parameters from our more moderate-resolution spectra a clear separation is not feasible. Therefore, for the Disk stars in this metallicity range, we adopt $[\alpha/\text{Fe}] \leq 0.2$ with the additional requirement that $|Z| < 650$ pc. Stars in the same parameter space with $|Z| > 650$ pc are assigned to the Thick Disk.

The Thick Disk. Stars with $[\alpha/\text{Fe}] > 0.2$ and $[\text{Fe}/\text{H}]$ from -0.5 to -1.2 are assumed to belong primarily to the Thick Disk, but there will be some overlap with the MWTD at the low metallicity side of this range. Given our color cutoff and the effective temperature distribution, we expect that most of the Thick Disk stars are near the main sequence turnoff. Adopting the corresponding luminosity, $M_v \approx +5.6$ mag, as a maximum luminosity, the faintest ($m_v \sim 19$ mag) and most distant Thick Disk stars would be expected to be no more than 5 kpc from the Sun. We therefore use this distance limit to select a sample of probable Thick Disk stars. For those stars with $[\text{Fe}/\text{H}] < -0.8$, we also add the requirement

that $|Z|$ is less than 2.0 kpc, approximately twice the vertical scale for the nominal Thick Disk (Larsen & Humphreys 2003), to roughly separate them from possible MWTD stars which have a higher scale height.

These criteria for the Disk and Thick Disk leave two orphan populations: a.) stars with $[\text{Fe}/\text{H}] > -0.5$ and $[\alpha/\text{Fe}] > 0.2$, and b.) stars with $[\text{Fe}/\text{H}] -0.5$ to -1.2 and $[\alpha/\text{Fe}] < 0.2$. For group a, stars with $[\alpha/\text{Fe}] > 0.3$ are assigned to the Thick Disk according to the above criteria. For the few with $[\alpha/\text{Fe}]$ between 0.2 and 0.3, those with $|Z| < 650$ pc are placed with the Disk stars. Since there are very few Disk stars with $[\text{Fe}/\text{H}]$ below -0.5, group b stars are treated with the same criteria as the Thick Disk, and any in the lower metallicity range, $[\text{Fe}/\text{H}] < -0.8$, with $|Z| > 2$ kpc are assigned to the MWTD.

For those stars that do not have an $[\alpha/\text{Fe}]$ measurement, but with an $[\text{Fe}/\text{H}]$ that would place them in either the Disk or Thick Disk, we adopted the $[\text{Fe}/\text{H}]$ separation from Parker et al. (2004) at -0.3 . All with $[\text{Fe}/\text{H}]$ between -0.3 and -0.5 and distances ≤ 5 kpc were assigned to the Thick Disk. Those with $[\text{Fe}/\text{H}]$ between 0 and -0.3 and $|Z| < 650$ pc are assumed to be in the Disk, and those $|Z| > 650$ pc and closer than 5 kpc, in the Thick Disk.

The Metal-Weak Thick Disk. Carollo et al. (2010) conclude that the MWTD contributes a significant number of stars in the metallicity range $-1.8 < [\text{Fe}/\text{H}] < -0.8$ which also includes Thick Disk and Inner Halo stars. They also find that the MWTD has a much higher scale height than the Thick Disk. Therefore for stars with $[\text{Fe}/\text{H}]$ from -0.8 to -1.2 , we adopt a $|Z|$ distance of 2 kpc for an approximate separation of the MWTD and the Thick Disk as described above. Stars with $[\text{Fe}/\text{H}] < -1.2$ and $|Z| > 4$ kpc are assigned to the Halo. For this study we do not attempt to separate the Inner and Outer Halo. All stars with $[\text{Fe}/\text{H}] < -1.8$ are assigned to our Halo population.

The population criteria are summarized in Table 3. Given our adopted criteria

together with the resolution of the abundance parameters, there will undoubtedly be some contamination and overlap among these groups. For this reason we use V_{LSR} to further refine the population separation. There are several stars in the Thick Disk and MWTD samples with V_{LSR} 's close to our high-velocity cutoff. Most of these same stars have $[Fe/H]$ values that would place them in the population overlap. For that reason we assigned stars with $V_{LSR} \geq 150 \text{ km s}^{-1}$ to the Halo. The resulting mean values with their errors plus the mean $[Fe/H]$ for each population are given in Table 4. The high-velocity stars with $V_{LSR} > 200 \text{ km s}^{-1}$ are also listed in Table 4. They are presumably members of the Halo but were not included in the four population groups.

5. The Kinematic Asymmetry and Rotational Lag

The mean velocities and rotation rates between Q1 and Q4 in Table 4 for the Thick Disk, MWTD, and Disk stars confirm the symmetry in the kinematics in Q1 above and below the plane, as well as our previous conclusion that a significant population of Q1 stars are rotating slower than those in Q4. In Q1 the shift to more negative velocities and the rotational lag is quite apparent for the Thick Disk population, confirming the kinematic asymmetry between Q1 and Q4. The Disk population in Q1 also appears to be participating in the rotational lag to some extent. The Q1 Disk stars above the plane have a significant negative V_{LSR} compared to the slightly positive velocity for the stars below the plane. However, as we noted previously, there are significantly more Disk stars in Q1B and in Q4 which may yield a more representative result for these two regions. Nevertheless, both regions in Q1 exhibit a slower rotational rate (ω) relative to Q4. Given our population selection criteria, however, there is the possibility that a number of Thick Disk stars are included within this group. As a test, we restricted our Disk population to stars with $[Fe/H] > 0$ and within 2 kpc of the Sun to get a sample more likely to be Disk stars only.

We obtain a negative mean V_{LSR} of $-8.9 \pm 7.5 \text{ km s}^{-1}$ in Q1. Although there were only 21 stars and the uncertainty is large, this result supports our conclusion that the Disk stars in Q1 also show the kinematic asymmetry.

The MWTD shows the same asymmetry between Q1 and Q4 and evidence for an even larger lag with a much smaller rotational rate than for the Thick Disk. The results for the MWTD in Q4 also suggest a greater lag, or shift to more positive velocities and smaller ω , relative to the corresponding Q4 Thick Disk stars. The MWTD stars also have a higher velocity dispersion than the Thick Disk. The results for the Halo stars are much as we would expect for a slowly moving, retrograde population with a high velocity dispersion with respect to the LSR.

The results for the individual fields are in Appendix C. The four paired fields across the $b = 0$ line yield self-consistent results for the populations, demonstrating the symmetry in Q1. Earlier we mentioned what appeared to be an anomalously negative velocity distribution for H048-45 which one can see reflected in the numbers for this field in Appendix C. The other characteristics of this field, such as its metallicity distribution, appear to be normal. The region of the sky containing this field is included in the SDSS-DR7 and SEGUE1. We examined the data in the direction of H048-45 and found several stars, selected by our criteria, with the same high velocities. On this basis, we conclude that our measured velocities are not in error or due to instrument or calibration errors. Furthermore, our line of sight toward H048-45 does not appear to intersect a known cluster, dwarf galaxy or star stream, but given the abundance of fossil remnants and streams in the Halo, this field is not included in the above analysis or the remaining discussion. Its inclusion would not alter the conclusions.

To determine the actual rotational lag, we must measure the velocity component in the direction of Galactic rotation, or the circular velocity. The observed V_{LSR} is a

combination of the stars’ motions in the radial (v_r), tangential (v_ϕ), and vertical (v_z) directions. Assuming that the stellar populations have a common or shared motion in their respective regions, we use the Levenberg-Marquardt technique (Levenberg 1944; Marquardt 1963) for non-linear least squares with the equation

$$V_{LSR} = [v_r \cos\theta + R_* (\frac{v_\phi}{R_*} - \frac{V_\odot}{R_\odot}) \sin\theta] \cos b + v_z \sin b \quad (1)$$

where θ is the angle between the line of sight from the Sun to the star and the Galactic Center to the star, $\sin\theta = R_\odot \sin l / R_*$, and R_* is the distance of the star from the Galactic Center. We then solve for v_ϕ , v_r , and v_z for the stellar populations in Q1 and Q4. The results are summarized in Table 5. The solutions with all three parameters often gave results, especially for v_z , that were not realistic, ranging from -50 to +84 km s⁻¹, and with large errors. We concluded that v_z is not sufficiently constrained by our data and repeated the solutions with two parameters setting $v_z = 0$. We also include the results solving only for v_ϕ . A few of the two-parameter solutions yielded what we presume are anomalously large values for v_r , up to 40 km s⁻¹ with large errors, although, in most cases, v_ϕ was consistent with the three- and one-parameter solutions. The results for the Disk in Q1B did not converge. Although there are more Disk stars than in Q1A, they are all in three fields at $b = 20^\circ$, and there was insufficient leverage in latitude for a solution. The spatial coverage in Q1B is less uniform than in the other two regions, and the results are weighted by the three fields near the plane. We therefore include a combined result for Q1 in Table 5, and in the following discussion we emphasize the comparison of Q1 and Q1A with Q4.

The results for v_ϕ , for the Thick Disk and MWTD in both quadrants, exhibit the rotational lag with respect to circular rotation in the Disk, $V_\odot \sim 220$ km s⁻¹, and relative to their respective solutions for the Disk. The solutions for the Thick Disk in Q1 are robust, irrespective of the number of parameters, and indicate a rotational lag of 60 to 70

km s⁻¹ relative to circular rotation and 20 to 30 km s⁻¹ slower than the Thick Disk stars in Q4, which have a net lag of ≈ 40 km s⁻¹, as expected for the canonical Thick Disk. The MWTD stars in Q1 have a significantly greater rotational lag of ≈ 100 km s⁻¹, 30 km s⁻¹ slower than for the Thick Disk. The solutions in Q4 for the MWTD, however, suggest a smaller lag of ≈ 60 km s⁻¹, again about 30 km s⁻¹ slower than the corresponding Thick Disk population, and 40 km s⁻¹ less than for the MWTD in Q1. The results also confirm our earlier suspicion that the Disk stars in Q1 participate in the rotational lag in the first quadrant. They appear to lag circular rotation by ≈ 30 km s⁻¹ while the Q4 stars have the expected circular rotation for the Disk.

In summary, although there is considerable range in some of the solutions, the results confirm the kinematic asymmetry and slower rotational lag in Q1. All three populations lag their corresponding populations in Q4 by ≈ 30 km s⁻¹.

In the next section, we conclude with a comparison of the kinematic and spatial asymmetries in the Hercules Thick Disk Cloud and its relationship to the bar in the Disk.

6. The Hercules Cloud and the Kinematic Asymmetry: Interaction with the Bar

In Paper II, Larsen et al. (2010b) confirm the over-density in Q1 among the faint blue stars and argue convincingly that it is due primarily to the Thick Disk stars. The star count excess is strongest above the plane between longitudes 20° to 50° and at higher latitudes. They conclude that, while still present at the lower latitudes, the signature is weaker, most likely due to the increased contribution from the Disk along the line of sight. One of the goals of the deeper photometric survey was to map the asymmetry along the line of sight to determine its full spatial extent. Larsen et al. (2010b) find that they can indeed identify

the feature’s far side at about 5 kpc from the Sun, where the star count ratios between Q1 and Q4 return to near one along the same sight lines. Significantly, the regions showing the strongest excess are over the near side of the density contours of the bar in the Disk and appear to be associated with the increasing density of the bar along the sight lines.

The stars included in our velocity survey were selected by the same criteria in color and magnitude range, and in most cases from the same fields in l and b on the sky as the stellar population exhibiting the over-density. These are the same populations. Thus, the stars showing the excess also participate in the kinematic asymmetry and the rotational lag. Comparing the kinematic results for the individual fields in Appendix C, we find that the asymmetry and lag for the Thick Disk stars exists across the entire region, in Q1 above and below the plane. Paired fields across the $b = 0$ line give very similar results. The kinematics thus parallel the star count excess. Compared with the over-density in Paper II, the kinematic asymmetry extends slightly beyond its apparent boundaries to 60° in two fields both at 20° in latitude.

The star counts suggest that we see *through* the Hercules Cloud to its far side at distances on the order of 5 kpc or greater. Although, our observations of the Thick Disk stars are limited to within 5 kpc of the Sun, and there are few stars at distances beyond 4 kpc, we also examined the apparent lag as function of distance along the line of sight. Figure 10 shows the variation in the mean V_{LSR} with distance. These two quantities appear to be correlated for large r . The mean V_{LSR} appears to shift to less negative values at greater distances, but the samples are too small to quantify the relation well. There are two immediate questions: (1) Is the correlation real? (2) Is it smooth, or is there a roughly constant velocity for $r < 4$ kpc followed by a rapid increase beyond that point? The issue is doubtful because the two uppermost points in the figure have much weaker statistical weight than those around $r \sim 2$ kpc. A statistical assessment suggests that the overall trend

is *most likely* real, but the confidence level is only in the 75–80% range, and the available data do not allow us to estimate the functional form. For example, a linear fit for $r > 1$ kpc, and a very different two-velocity model with $V_{LSR} \sim \text{constant}$ out to 4 kpc, are about equally successful.⁸

We probably see through Hercules Cloud to its far side at $r \gtrsim 4$ kpc. The mean V_{LSR} may or may not be increasing between $r \sim 1$ kpc and 4 kpc, but V_{LSR} does appear to increase at greater distances. This suggests that the rotational lag is less at larger distances, as our line of sight apparently passes through the Cloud to its far side, as in the case of the star counts. The only caveat is that, at greater distances, our lines of sight are also at higher $|Z|$ distances from the plane. For the Thick Disk stars in Q1, most of the stars at more than 4 kpc are 1.5 to 2 kpc above the plane. This trend is not as apparent for the MWTD with fewer stars per distance bin and a higher velocity dispersion. This pattern for the Thick Disk corresponds very well with the over-density and star count excess discussed in Paper II.

With the addition of velocities for fainter stars we have traced the kinematic asymmetry and the enhanced rotational lag for the Thick Disk stars in Q1 out to 4 kpc or more. The

⁸ A standard weighted linear fit to $V_{LSR}(r)$ for $r > 1$ kpc has slope = -1.9 ± 1.7 km s⁻¹ per kpc. Hence the existence of a positive slope is roughly an 88%-confidence hypothesis. We try three simple models: (a) a constant $V_{LSR} = -16.5$ km s⁻¹; (b) the linear fit; and (c) a two-value model with $V_{LSR} = -17.1$ km s⁻¹ for $r < 4$ kpc and -5.9 km s⁻¹ for $r > 4$ kpc. The chi-squared sums (4.49, 3.29, and 1.73 respectively) indicate that all three models are plausible within the known statistical errors, but model (c) fits best even if we allow for the fact that it has three adjustable parameters. Model (a) is noticeably poorer by the same standard. Intermediate functional forms give similar results. Note that the data for Figure 10 is available on-line with the figure.

rotational lag is greatest along our lines of sight toward the bar in the Disk. At 3 to 4 kpc our sight lines extend above the density contours mapped by the AGB stars on the near side of the bar (Weinberg 1992), but as our line of sight passes directly over the bar, the rotational lag appears to decrease. The kinematics are consistent with a “gravitational wake” induced by the rotating bar in the Disk that would trap and pile up stars *behind* it (Hernquist & Weinberg 1992; Debattista & Sellwood 1998). Furthermore, the kinematic asymmetry and slower rotational lag in Q1 is shared by all three stellar populations, the Thick Disk, MWTD, and the Disk. Interestingly, we find that the additional lag, relative to the same populations in Q4, is comparable for all three, at about 30 km s^{-1} . The net rotational lag in the direction of the bar for the stellar populations together with the over-density, above and below the plane, support a dynamical interaction with the bar as the most likely explanation. This conclusion does not necessarily eliminate the role of a merger remnant which could be interacting with the bar. However, the common stellar parameters, such as metallicity, demonstrate that the populations in Q1 and Q4 are the same, with asymmetric spatial and kinematic properties, not two different populations.

Future work should include dynamical modeling of the interaction with the bar and extended observations of more stars at the fainter magnitudes to trace the kinematics to greater distances across the bar.

This work was supported by Collaborative National Science Foundation grants to Humphreys (AST0507170), Cabanela (AST0729989), and Larsen (AST0507309). They thank the MMT Observatory, the support staff for the Hectospec and the telescope operators, and NOAO and the staff at CTIO for excellent observing support. Beers and Lee acknowledge partial funding of this work from grants PHY 02-16783 and PHY 08-22648: Physics Frontier Center/Joint Institute for Nuclear Astrophysics (JINA), awarded by the U.S. National Science Foundation.

Facilities: MMT/Hectospec, Bok/90Prime, CTIO/SMARTS/1.0m, CTIO/Blanco/Hydra

A. Catalog of Velocities, Metallicities, and Atmospheric Parameters

The Catalog of velocities, metallicities, and the atmospheric parameters with their errors are available as an on-line supplement to this paper. Table A1 includes all of the stars with V and B-V magnitudes and colors (Papers I and II). Table A2 is for those stars which only have photographic O and O-E magnitudes and colors from the Minnesota Automated Plates Scanner Catalog of the POSS I. It includes the stars from Parker et al. (2004). Examples are shown in Tables A1 and A2. The Catalog is also available at <http://aps.umn.edu>.

B. Mean V_{LSR} and Rotation Rates for the Individual Fields in Q1 and Q4

C. Mean V_{LSR} and Rotation Rates for the Different Populations in the Individual Fields

REFERENCES

- Abazajian, K. N., Adelman-McCarthy, J. K., Agüeros, M. A., et al. 2009, *ApJS*, 182, 543
- Allende Prieto, C., Sivarani, T., Beers, T. C., et al. 2008, *AJ*, 136, 2070
- Abadi, M. G., Navarro, J. F., Steinmetz, M., & Eke, V. R. 2003, *ApJ*, 597, 21
- Beers, T. C., Chiba, Masashi; Y., Y., Platais, I., Hanson, R. B., Fuchs, B., & Rossi, S. 2000, *AJ*, 119, 2866
- Belokurov, V., et al. 2007, *ApJ*, 657, L89
- Bensby, T., Zenn, A. R., Oey, M. S., & Feltzing, S. 2007, *ApJ*, 663, 13
- Bensby, T., Feltzing, S. & Lundstrom, I. 2003, *A&A*, 410, 527
- Bensby, T., Feltzing, S. & Lundstrom, I. 2004, *A&A*, 415, 155
- Blitz, L., & Spergel, D. N. 1991, *ApJ*, 379, 631
- Brand, J. & Blitz, L., 1993, *A&A*, 275, 67
- Cabanela, J. E., Humphreys, R. M., Aldering, G., Larsen, J. A., Odewahn, S. C., Thurmes, P. M., & Cornuelle, C. S. 2003, *PASP*, 115, 837
- Carollo, D., Beers, T. C., Chiba, M., Norris, J. E., Freeman, K. C., Lee, Y. S., Ivezić, Z., Rockosi, C. M., & Yanny, B. 2010, *ApJ*, 712, 692
- Chiba, M. & Beers, T. C. 2000, *AJ*, 119, 2843
- Cutri, R. M., Skrutskie, M. F., van Dyk, S., et al. 2003, *2MASS All Sky Catalog of Point Sources*, ed. Cutri, R. M., et al.
- Debattista, V. P., & Sellwood, J. A. 1998, *ApJ*, 493, L5

- Fabricant, D. G., Hertz, E. N., Szentgyorgyi, A. H., Fata, R. G., Roll, J. B. & Zajac, J. M. 1998, Proc. SPIE, 3355, 285
- Feltzing, S. & Bensby, T. 2008, Physica Scripta, Volume 133, Issue , pp. 014031
- Hammersley, P. L., Garzón, F., Mahoney, T. J., López-Corredoira, M., & Torres, M. A. P. 2000, MNRAS, 317, L45
- Hernquist, L., & Weinberg, M. D. 1992, ApJ, 400, 80
- Ibata, R.A., Wyse, R.F., Gilmore, G., Irwin, M.J. & Suntzeff, N. B., 1997, AJ, 113, 634.
- Jordi, K., Grebel, E. K., & Ammon, K. 2006, A&A, 460, 339
- Larsen, J. A., & Humphreys, R. M. 1996, ApJ, 468, L99
- Larsen, J. A., & Humphreys, R. M. 2003, AJ, 125, 1958
- Larsen, J. A., Humphreys, R. M., & Cabanela, J. E. 2008, ApJ, 687, L17
- Larsen, J. A., Humphreys, R. M., Cabanela, J. E. & Haviland, A. P. 2010a, AJ, 139, 348
- Larsen, J. A., Cabanela, J. E. & Humphreys, R. M. 2010b, submitted to AJ
- Lee, Y. S., Beers, T. C., Sivarani, T., et al. 2008a, AJ, 136, 2022
- Lee, Y. S., Beers, T. C., Sivarani, T., et al. 2008b, AJ, 136, 2050
- Lee, Y. S., et al. 2010, AJ, in press
- Levenberg, K. 1944, The Quarterly of Applied Mathematics, 2, 164
- Marquardt, D. 1963, SIAM Journal of Applied Mathematics, 11, 431
- Nissen, P. E., Primas, F., Apslund, M. & Lambert, D. L. 2002, A&A, 390, 235

Parker, J. E., Humphreys, R. M., & Larsen, J. A. 2003, AJ, 126, 1346

Parker, J. E., Humphreys, R. M., & Beers, T. C. 2004, AJ, 127, 1567

Reid, I.N., 1998, AJ, 115, 4

Schlegel, D. J., Finkbeiner, D. P., & Davis, M. 1998, ApJ, 500, 525

Weinberg, M. D. 1992, ApJ, 384, 81

Wyse, R. F. G. 2009, in “The Galaxy Disk in Cosmological Context”, Proceedings of IAU
Symposium 254, ed. J. Andersen, J. Bland-Hawthorn, and B. Nordström, p. 179

York, D. G., Adelman, J., Anderson, Jr., J. E., et al. 2000, AJ, 120, 1579

Table 1. Observations

Field	l [°]	b [°]	Stars with velocities	Total Exp Time [min]	Dates Observed
CTIO/Hydra 2006 ^a					
P802	339.5	33.0	96	120	May 04, 05
P855	309.0	37.0	73	120	May 05
P858	329.0	32.0	95	120	May 04
P910	303.0	30.0	71	120	May 04
P913	320.0	30.0	94	120	May 05
CTIO/Hydra 2008 ^b					
H333+37	333.0	37.0	103	280	Apr 08,10
H330+20	330.0	20.0	96	240	Apr 06,07,08,09,10
H327+40	327.0	40.0	105	250	Apr 08,09
H312+45	313.0	45.0	94	300	Apr 07,09,10
H310+31	310.0	31.0	64	300	Apr 07,08,10
H305+42	305.0	42.0	84	300	Apr 06,08,09
MMT/Hectospec ^b 2007 & 2008					
H020+32	21.0	32.0	166	150	Jun 13, 2007
H027+37	28.0	37.0	230	150	May 31, 2008
H030+20	31.0	20.0	187	150	Jun 15,19, 2007
H030-20	31.0	-20.0	250	150	Oct 17,2007,Sep 08,2008
H033+40	33.0	40.0	229	150	Jun 01, 2008
H035+32	36.0	32.0	178	150	May 14, Oct 14, 2007
H035-32	36.0	-32.0	184	150	Jun 16,19 2007
H045-20	46.0	-20.0	210	150	Oct 18, 2007
H048-45	49.0	-44.0	199	150	Sep 09, 2008
H050+31	51.0	31.0	176	150	Jun 13, Oct 18, 2007
H050-31	51.0	-31.0	161	120	Jun 18, 2007
H060+20	61.0	20.0	209	90	Oct 15, 2007
H060-20	61.0	-20.0	215	150	Oct 14, 2007

^aRepeat of some fields observed by Parker et al. (2004). We use the same field identifications from the MAPS.

^bInformation for these fields is in (Larsen et al. 2010a).

Table 2. Mean V_{LSR} Velocities and Rotation Rates^a

Quadrant	N_{stars}	$\langle V_{LSR} \rangle$ km s ⁻¹	$\sigma_{V_{LSR}}$ km s ⁻¹	$\langle \omega \rangle$ km s ⁻¹ kpc ⁻¹	σ_{ω} km s ⁻¹ kpc ⁻¹
Q1 above	1679	-28.6 ± 1.6	66.4	19.6 ± 0.5	21.0
Q1 below	1135	-35.6 ± 2.0 ^b	67.4	19.7 ± 0.5 ^b	15.3
Q4 above	1170	-11.6 ± 2.0	66.7	31.3 ± 0.6	20.4

^aStars with V_{LSR} greater than ± 200 km s⁻¹ are excluded from the determination of the mean V_{LSR} and mean ω .

^bWithout H048-45 (see text), $\langle V_{LSR} \rangle$ and $\langle \omega \rangle$ for Q1 below the plane are, respectively, -22.6 km s⁻¹ and 22.9 km s⁻¹kpc⁻¹.

Table 3. Criteria for Population Separation

Population	[Fe/H]	$[\alpha/\text{Fe}]$	$ Z $	r_*
Disk	≥ 0	...	≤ 650 pc	...
	0 to -0.3^{a}	...	≤ 650 pc	...
	0 to -0.5	≤ 0.2	≤ 650 pc	...
	0 to -0.5	0.2 to 0.3	≤ 650 pc	...
Thick Disk	0 to -0.3^{a}	...	> 650 pc	≤ 5 kpc
	-0.3 to -0.5^{a}	≤ 5 kpc
	0 to -0.5	< 0.3	> 650 pc	≤ 5 kpc
	0 to -0.5	> 0.3	...	≤ 5 kpc
	< -0.5 to -0.8	≤ 5 kpc
	-0.8 to -1.2	...	< 2 kpc	≤ 5 kpc
MWTD	< -0.8 to -1.2	...	$\leq 2 Z \leq 4$ kpc	...
	-1.2 to -1.8	...	< 4 kpc	...
Halo	-1.2 to -1.8	...	≥ 4 kpc	...
	< -1.8

^aUsed for stars without an $[\alpha/\text{Fe}]$ estimate. See text

Table 4. Mean [Fe/H], LSR Velocities and Rotation Rates for the Four Populations

Population	N_{stars}	[Fe/H]	$\langle V_{LSR} \rangle$ km s ⁻¹	$\sigma_{V_{LSR}}$ km s ⁻¹	$\langle \omega \rangle$ km s ⁻¹ kpc ⁻¹	σ_{ω} km s ⁻¹ kpc ⁻¹
Disk						
Q1A	39	-0.3	-14.0 ± 5.5	34.2	24.4 ± 1.2	7.2
Q1B	105	-0.2	0.3 ± 3.5	35.9	27.6 ± 0.8	7.7
Q4	70	0.0	-19.9 ± 4.1	34.5	32.3 ± 1.0	8.7
Thick Disk						
Q1A	793	-0.8	-18.4 ± 1.9	52.2	23.2 ± 0.5	15.3
Q1B	453	-0.7	-12.5 ± 2.3	49.4	25.0 ± 0.5	10.4
Q4	555	-0.7	-20.1 ± 2.3	53.5	33.5 ± 0.7	15.6
MWTD						
Q1A	379	-1.3	-25.2 ± 3.5	61.6	20.1 ± 1.0	19.9
Q1B	117	-1.4	-41.0 ± 5.7	61.5	19.2 ± 1.2	13.2
Q4	216	-1.3	-10.2 ± 4.5	65.7	31.6 ± 1.4	20.7
Halo						
Q1A	337	-1.8	-82.7 ± 4.9	90.3	3.0 ± 1.6	29.4
Q1B	108	-1.9	-88.9 ± 9.7	100.7	9.5 ± 2.2	22.7
Q4	103	-1.9	48.0 ± 11.3	115.0	15.3 ± 3.6	36.3
High Velocity ^a						
Q1A	117	-1.6	-238.5 ± 11.0	118.6	-35.2 ± 4.0	43.4
Q1B	66	-1.6	-281.8 ± 6.2	50.6	-30.2 ± 1.9	15.6
Q4	29	-1.4	209.1 ± 34.1	183.8	-25.1 ± 9.1	48.9

^aThe high velocity stars ($V_{LSR} \geq \pm 200$ km s⁻¹) were not included in the four populations. They are listed separately here although, they are presumably members of the Halo.

Table 5. Solutions for the Velocity Components

Population	N_{stars}	v_r km s ⁻¹	v_ϕ km s ⁻¹	v_z km s ⁻¹	σ km s ⁻¹
Disk					
Q1	145	0 ± 10	193 ± 8	-19 ± 8	35
		-3 ± 10	194 ± 8	(0)	36
		(0)	196 ± 4	(0)	36
Q1A	40	+12 ± 50	194 ± 15	-7 ± 57	36
		+18 ± 20	193 ± 14	(0)	36
		(0)	183 ± 8	(0)	36
Q1B	105	-177 ± 97	408 ± 118	+721 ± 405	35
		-5 ± 11	198 ± 9	(0)	35
		(0)	202 ± 5	(0)	35
Q4	69	+34 ± 29	220 ± 34	+18 ± 57	35
		+27 ± 19	211 ± 20	(0)	35
		(0)	237 ± 7	(0)	35
Thick Disk					
Q1	1245	-2 ± 5	161 ± 4	-14 ± 3	50
		+7 ± 5	165 ± 4	(0)	51
		(0)	161 ± 2	(0)	51
Q1A	793	-27 ± 11	169 ± 7	-50 ± 15	51
		+4 ± 6	155 ± 5	(0)	51
		(0)	152 ± 3	(0)	51
Q1B	452	-32 ± 12	196 ± 9	+84 ± 24	49
		-3 ± 9	169 ± 5	(0)	49
		(0)	171 ± 3	(0)	50
Q4	551	+43 ± 11	182 ± 12	+2 ± 16	54
		+42 ± 9	181 ± 8	(0)	53
		(0)	217 ± 4	(0)	54

MWTD

Table 5—Continued

Population	N_{stars}	v_r km s ⁻¹	v_ϕ km s ⁻¹	v_z km s ⁻¹	σ km s ⁻¹
Q1	492	-13 ± 12	113 ± 7	-8 ± 7	63
		-7 ± 10	115 ± 7	(0)	63
		(0)	119 ± 4	(0)	63
Q1A	377	-24 ± 19	136 ± 14	-43 ± 25	64
		+2 ± 12	120 ± 10	(0)	64
		(0)	118 ± 5	(0)	64
Q1B	115	-46 ± 26	103 ± 30	+5 ± 56	60
		-45 ± 22	100 ± 12	(0)	60
		(0)	120 ± 7	(0)	61
Q4	216	-1 ± 22	138 ± 24	-49 ± 36	64
		+21 ± 15	165 ± 13	(0)	64
		(0)	181 ± 7	(0)	64

Table A1. Catalog of Velocities, Metallicity, and Atmospheric Parameters (CCD
Photometry)

Object	l deg	b deg	V mag	$B - V$ mag	V_{Hel} km s ⁻¹	V_{LSR} km s ⁻¹	ω km s ⁻¹ kpc ⁻¹	[Fe/H]	[α /Fe]	T_{eff} °K	logg	Dist. kpc
H060+20-022532	60.54	+19.99	18.68	+0.59	-56.6(4.1)	-40.2	+21.4	-1.01(0.02)	+0.24(0.04)	5691(34)	3.87(0.35)	3.0
H060+20-020900	60.53	+20.03	18.39	+0.60	+2.4(4.6)	+18.8	+30.4	-0.43(0.02)	+0.18(0.04)	5683(82)	4.36(0.28)	2.3
H060+20-018959	60.50	+20.07	17.10	+0.73	-400.3(2.7)	-383.9	-31.2	-1.01(0.03)	+0.30(0.04)	5702(61)	4.19(0.40)	2.2
H060+20-018109	60.48	+20.22	16.30	+0.63	-322.2(3.6)	-305.9	-19.3	-1.03(0.02)	+0.02(0.06)	5896(39)	3.97(0.25)	4.0
H060+20-015828	60.47	+20.29	16.82	+0.74	+16.6(1.7)	+32.9	+32.5	-2.19(0.05)	+0.08(0.06)	5341(40)	3.02(0.08)	3.7
H060+20-023202	60.46	+19.95	18.16	+0.73	+43.0(3.0)	+59.4	+36.6	-0.70(0.05)	+0.12(0.03)	5720(53)	3.70(0.43)	1.0

Table A2. Catalog of Velocities, Metallicity, and Atmospheric Parameters (MAPS
Photometry)

Object ^a	l deg	b deg	O mag	$O - E$ mag	V_{Hel} km s ⁻¹	V_{LSR} km s ⁻¹	ω km s ⁻¹ kpc ⁻¹	[Fe/H]	[α /Fe]	T_{eff} °K	logg	Dist. kpc
P332-1931756	51.26	+37.07	15.89	+0.43	+12.5(3.6)	+28.6	+33.2	-0.09(0.08)	-0.01(0.05)	5430(31)	3.90(0.56)	2.4
P332-1925176	51.21	+37.31	15.56	+0.57	-66.4(5.5)	-50.3	+17.4	-0.74(0.03)	+0.47(0.02)	5349(19)	4.88(0.17)	1.3
P332-1922793	51.12	+37.37	15.79	+0.35	-84.8(9.9)	-68.7	+13.6	-0.34(0.02)	+0.26(0.03)	5596(29)	4.08(0.01)	3.7
P332-1923351	51.11	+37.35	15.98	+0.47	-72.8(2.9)	-56.7	+16.1	-1.20(0.10)	+0.51(0.03)	5343(51)	4.53(0.06)	2.2
P332-1925685	51.09	+37.26	16.12	+0.53	-55.6(1.7)	-39.5	+19.5	-0.63(0.04)	+0.38(0.02)	5455(80)	4.88(0.11)	1.8
P332-2071813	51.04	+36.98	15.77	+0.46	-32.6(2.9)	-16.4	+24.2	-2.53(0.18)	+0.11(0.08)	6370(38)	3.07(0.36)	2.3

^aThe stars in this table are from the Minnesota Automated Plate Scanner (MAPS) Catalog of the POSS I. Their complete designation is "MAPS-PXXX-YYYYYY".

Table B. Mean LSR Velocities and Rotation Rates for Individual Fields in Q1 and Q4^a

Field	l, b	N_{stars}	$\langle V_{LSR} \rangle$ km s ⁻¹	$\sigma_{V_{LSR}}$ km s ⁻¹	$\langle \omega \rangle$ km s ⁻¹ kpc ⁻¹	σ_{ω} km s ⁻¹ kpc ⁻¹
Q1 above						
H060+20	61.0, 20.0	193	-33.9 ± 3.8	52.9	22.3 ± 0.6	8.4
P332	51.0, 37.0	37	-45.8 ± 9.2	56.0	18.2 ± 1.9	11.3
H050+31	51.0, 31.0	157	-50.6 ± 4.2	55.9	17.9 ± 0.8	10.6
P387	40.0, 41.0	57	-35.0 ± 7.6	57.8	18.4 ± 2.0	15.0
P448	40.0, 30.0	60	-15.9 ± 8.1	63.4	23.9 ± 1.8	14.2
H035+32	36.0, 32.0	165	-32.1 ± 5.2	67.3	19.3 ± 1.4	17.3
H033+40	33.0, 40.0	217	-31.8 ± 4.2	62.5	17.8 ± 1.3	19.0
P507	31.0, 32.0	65	-20.7 ± 8.6	69.5	21.6 ± 2.5	20.0
H030+20	31.0, 20.0	174	-12.6 ± 5.9	78.4	24.2 ± 1.6	20.9
H027+37	28.0, 37.0	219	-25.3 ± 4.8	70.9	18.8 ± 1.7	24.4
P505	21.0, 42.5	62	-26.2 ± 8.5	67.2	15.0 ± 4.0	32.0
H020+32	21.0, 32.0	273	-20.9 ± 4.3	70.2	18.5 ± 1.8	30.2
Q1 below						
H060-20	61.0, -20.0	202	-29.8 ± 3.8	54.4	22.9 ± 0.6	8.1
H050-31	51.0, -31.0	139	-52.5 ± 6.1	72.1	17.5 ± 1.2	13.7
H048-45	49.0, -44.0	182	-104.1 ± 3.5	46.6	2.5 ± 0.8	11.2
H045-20	46.0, -20.0	198	-8.9 ± 4.2	58.7	25.8 ± 0.8	11.0
H035-32	36.0, -32.0	169	-23.9 ± 5.3	69.0	21.3 ± 1.4	17.8
H030-20	31.0, -20.0	245	-9.8 ± 3.5	55.3	24.9 ± 0.9	14.7
Q4 above						
P910	303.0, 30.0	69	-0.9 ± 6.7	55.4	27.6 ± 1.2	9.6
H305+42	305.0, 42.0	80	5.0 ± 6.3	56.7	26.5 ± 1.3	12.5
P855	309.0, 37.0	78	3.9 ± 6.2	54.8	26.7 ± 1.3	11.1
H310+31	310.0, 31.0	64	8.7 ± 8.2	65.5	25.8 ± 1.6	12.5
H312+45	313.0, 45.0	93	-5.4 ± 6.1	58.8	28.8 ± 1.5	14.1
P799	320.0, 41.0	60	-8.8 ± 8.6	66.6	29.8 ± 2.2	17.2
P913	320.0, 30.0	120	-22.4 ± 4.9	53.3	32.5 ± 1.1	12.0

Table B—Continued

Field	l, b	N_{stars}	$\langle V_{LSR} \rangle$ km s ⁻¹	$\sigma_{V_{LSR}}$ km s ⁻¹	$\langle \omega \rangle$ km s ⁻¹ kpc ⁻¹	σ_{ω} km s ⁻¹ kpc ⁻¹
H327+40	327.0, 40.0	103	-6.3 ± 7.3	74.5	29.4 ± 2.2	22.3
P858	329.0, 32.0	114	-9.4 ± 6.1	65.5	30.2 ± 1.8	18.9
H330+20	330.0, 20.0	93	-40.4 ± 7.3	70.5	38.3 ± 2.0	18.8
H333+37	333.0, 37.0	101	1.6 ± 7.4	74.7	26.9 ± 2.6	25.7
P741	339.0, 41.0	63	-33.3 ± 8.3	66.0	42.8 ± 3.8	30.3
P802	339.5, 33.0	122	-28.5 ± 5.7	63.1	39.5 ± 2.4	26.8

^aStars with V_{LSR} greater than ± 200 km s⁻¹ are excluded from the determination of the mean V_{LSR} and mean ω .

Table C. Kinematics for the Populations in the Individual Fields

Field	l/b	N_{stars}	$\langle V_{LSR} \rangle$ km s ⁻¹	$\sigma_{V_{LSR}}$ km s ⁻¹	$\langle \omega \rangle$ km s ⁻¹ kpc ⁻¹	σ_{ω} km s ⁻¹ kpc ⁻¹
Q1 above						
H060+20	61/+20					
Disk		21	-11.4 ± 8.2	37.8	25.7 ± 1.3	5.8
ThDi		118	-33.2 ± 4.6	49.9	22.4 ± 0.7	7.7
MWTD		24	-29.3 ± 10.4	50.9	23.0 ± 1.6	7.8
Halo		16	-59.0 ± 19.0	76.0	18.4 ± 2.9	11.7
P332	51/+37					
ThDi		27	-42.1 ± 9.6	49.9	18.9 ± 1.9	10.1
MWTD		4	-2.4 ± 18.5	37.1	27.0 ± 3.8	7.6
Halo		3	-110.8 ± 48.7	84.4	5.1 ± 9.9	17.1
H050+31	50/+31					
Disk		2	-47.4 ± 27.0	38.1	18.5 ± 5.1	7.3
ThDi		122	-35.8 ± 4.0	44.2	20.7 ± 0.8	8.4
MWTD		27	-47.0 ± 9.2	47.6	18.6 ± 1.7	9.0
Halo		29	-128.6 ± 10.4	56.3	3.1 ± 2.0	10.7
P387	40/+41					
ThDi		25	-22.7 ± 9.6	47.8	21.6 ± 2.5	12.3
MWTD		23	-39.5 ± 9.6	45.8	17.3 ± 2.5	11.83
Halo		9	-75.3 ± 33.1	99.3	7.8 ± 8.6	25.9
P448	40/+30					
ThDi		17	-20.0 ± 13.7	56.6	23.0 ± 3.1	12.7
MWTD		22	-13.3 ± 15.3	71.6	24.5 ± 3.4	16.1
Halo		12	-28.6 ± 20.8	72.2	21.0 ± 4.7	16.2
H035+32	36/+32					
ThDi		95	-8.0 ± 4.9	48.1	25.4 ± 1.3	12.4
MWTD		39	-28.1 ± 9.9	61.8	20.3 ± 2.5	15.9
Halo		31	-124.7 ± 11.0	61.5	-4.5 ± 2.8	15.8
H033+49	33/+40					
Disk		10	-16.1 ± 10.8	34.3	22.6 ± 3.3	10.5
ThDi		68	-24.9 ± 5.5	45.2	19.9 ± 1.7	13.8

Table C—Continued

Field	l/b	N_{stars}	$\langle V_{LSR} \rangle$ km s ⁻¹	$\sigma_{V_{LSR}}$ km s ⁻¹	$\langle \omega \rangle$ km s ⁻¹ kpc ⁻¹	σ_{ω} km s ⁻¹ kpc ⁻¹
MWTD		48	-18.8 ± 8.1	56.1	21.8 ± 2.5	17.1
Halo		65	-82.5 ± 10.2	82.0	2.5 ± 3.1	24.9
P507	31/+32					
ThDi		22	-6.4 ± 10.7	50.4	25.7 ± 3.1	14.5
MWTD		23	-36.6 ± 17.0	81.7	16.9 ± 4.9	23.4
Halo		10	-82.2 ± 28.9	91.3	3.9 ± 8.3	26.3
H030+20	30/+20					
Disk		3	-2.6 ± 2.8	4.8	26.8 ± 0.7	1.3
ThDi		86	8.5 ± 5.7	53.0	29.8 ± 1.5	14.1
MWTD		36	-19.0 ± 11.4	68.2	22.5 ± 3.0	18.2
Halo		36	-83.4 ± 19.7	118.4	5.2 ± 5.3	31.6
H027+37	28/+37					
Disk		3	-14.1 ± 12.6	21.8	22.7 ± 4.2	7.3
ThDi		86	-4.7 ± 5.7	52.6	25.9 ± 1.9	18.1
MWTD		50	-24.4 ± 8.8	62.2	19.1 ± 3.0	21.4
Halo		63	-74.1 ± 11.8	93.4	2.0 ± 4.0	32.1
P505	21/+42.5					
ThDi		19	-18.9 ± 13.2	57.6	18.6 ± 6.2	27.1
MWTD		27	-22.6 ± 12.2	63.3	16.7 ± 5.8	30.0
Halo		14	-52.7 ± 26.0	97.5	2.1 ± 12.5	46.9
H020+32	21/+32					
ThDi		108	-15.0 ± 5.4	56.5	21.0 ± 2.3	24.3
MWTD		56	-18.0 ± 8.6	64.3	19.7 ± 3.7	27.7
Halo		49	-68.7 ± 13.8	96.7	-2.1 ± 6.0	41.8
Q1 below						
H060-20	61/-20					
Disk		36	-9.7 ± 5.5	33.0	26.0 ± 0.8	5.1
ThDi		124	-21.8 ± 4.2	47.1	24.1 ± 0.6	7.2
MWTD		12	-65.8 ± 13.6	47.1	17.4 ± 2.1	7.2

Table C—Continued

Field	l/b	N_{stars}	$\langle V_{LSR} \rangle$ km s ⁻¹	$\sigma_{V_{LSR}}$ km s ⁻¹	$\langle \omega \rangle$ km s ⁻¹ kpc ⁻¹	σ_{ω} km s ⁻¹ kpc ⁻¹
Halo		14	-116.3 ± 21.8	81.8	9.7 ± 3.4	12.6
H050-31	51/-30					
ThDi		55	-19.0 ± 6.3	46.7	23.9 ± 1.2	8.9
MWTD		42	-50.4 ± 9.6	61.9	17.9 ± 1.8	11.8
Halo		33	-111.0 ± 15.4	88.3	6.4 ± 2.9	16.8
H048-45	49/-44					
Disk		1	-70.5	...	10.6	...
ThDi		91	-89.2 ± 3.9	37.6	6.1 ± 0.9	9.0
MWTD		16	-86.0 ± 9.5	38.0	6.9 ± 2.3	9.1
Halo		42	-159.1 ± 5.9	38.2	-10.8 ± 1.4	9.2
H045-20	45/-20					
Disk		26	16.3 ± 7.0	35.7	30.5 ± 1.3	6.7
ThDi		132	-1.4 ± 4.3	48.9	27.2 ± 0.8	9.2
MWTD		15	-44.3 ± 16.3	63.0	19.2 ± 3.1	11.8
Halo		18	-94.6 ± 18.4	78.0	9.7 ± 3.5	14.7
H035-32	35/-32					
ThDi		95	-17.1 ± 5.5	53.3	23.1 ± 1.4	13.7
MWTD		40	-23.5 ± 10.6	66.9	21.4 ± 2.7	17.3
Halo		31	-58.8 ± 20.2	112.7	12.4 ± 5.2	29.1
H030-20	31/-20					
Disk		43	-1.0 ± 5.5	35.8	27.2 ± 1.5	9.5
ThDi		48	-5.3 ± 7.2	49.7	26.1 ± 1.9	13.3
MWTD		8	-35.7 ± 7.2	20.4	18.0 ± 1.9	5.4
Halo		12	-65.2 ± 39.1	135.4	10.2 ± 10.4	35.9
Q4						
P910	303/+30					
Disk		11	-12.8 ± 11.1	36.8	29.7 ± 1.9	6.4
ThDi		43	-6.9 ± 6.7	43.9	28.7 ± 1.2	7.6
MWTD		9	12.4 ± 20.8	62.5	25.3 ± 3.6	10.8

Table C—Continued

Field	l/b	N_{stars}	$\langle V_{LSR} \rangle$ km s ⁻¹	$\sigma_{V_{LSR}}$ km s ⁻¹	$\langle \omega \rangle$ km s ⁻¹ kpc ⁻¹	σ_{ω} km s ⁻¹ kpc ⁻¹
Halo		3	115.4± 73.2	126.8	7.5± 12.7	21.9
H305+42	305/+42					
ThDi		40	-14.0± 7.0	44.4	30.4 ± 1.4	9.1
MWTD		8	17.3± 22.4	63.3	24.0 ± 4.6	13.0
Halo		11	90.6 ± 24.9	82.5	8.8 ± 5.1	17.0
P855	309/+37					
Disk		9	-6.3± 7.4	22.3	28.8± 1.5	4.5
ThDi		39	-2.6± 9.0	56.3	28.0± 1.8	11.4
MWTD		6	44.3± 29.5	72.3	18.5± 6.0	14.6
Halo		5	73.9±25.7	57.4	12.6± 5.2	11.6
H310+31	310/+51					
ThDi		39	-7.2± 8.6	53.5	28.9 ± 1.6	10.2
MWTD		16	2.2± 17.3	69.4	27.1± 3.3	13.3
Halo		4	127.1± 26.9	53.9	3.3 ± 5.1	10.2
H312+45	313/+45					
Disk		1	-37.9	...	27.4	...
ThDi		38	-19.9± 6.1	37.8	31.3 ± 1.5	9.1
MWTD		17	-13.0±16.6	68.5	30.6± 4.0	16.4
Halo		11	44.2± 19.7	65.2	16.9± 4.7	15.7
P799	320/+41					
ThDi		11	-2.7± 23.3	77.2	28.3± 6.0	19.9
MWTD		12	-15.0± 13.9	48.0	31.4± 3.6	12.4
Halo		2	-37.2 ± 2.4	3.3	37.1 ± 0.6	0.8
P913	320/+30					
Disk		22	-28.5± 5.6	26.2	33.9± 1.3	5.9
ThDi		65	-24.2± 6.6	53.3	32.9± 1.5	12.0
MWTD		12	-10.0± 21.1	73.2	29.8± 4.7	16.4
Halo		3	27.2± 63.6	110.1	21.5±14.2	24.6
H327+40	327/+40					
Disk		2	14.4± 30.2	42.7	23.2± 9.0	12.7
ThDi		52	-22.7± 8.6	62.2	34.3± 2.6	18.6

Table C—Continued

Field	l/b	N_{stars}	$\langle V_{LSR} \rangle$ km s ⁻¹	$\sigma_{V_{LSR}}$ km s ⁻¹	$\langle \omega \rangle$ km s ⁻¹ kpc ⁻¹	σ_{ω} km s ⁻¹ kpc ⁻¹
MWTD		24	-20.7± 9.3	45.6	33.7± 2.8	13.7
Halo		15	70.4± 30.2	117.0	6.3± 9.0	35.0
P858	329/+32					
Disk		22	-24.2± 8.0	37.6	34.5± 2.3	10.9
ThDi		54	-16.4± 6.6	48.7	32.2±1.9	14.0
MWTD		18	6.0±18.4	77.9	25.8± 5.3	22.6
Halo		9	78.2± 32.6	97.7	4.8± 9.4	28.3
H330+20	330/+20					
Disk		3	-8.9± 43.4	75.1	29.9±11.5	19.9
ThDi		54	-47.4± 8.4	61.5	40.1±2.2	16.4
MWTD		11	-34.5± 26.0	86.1	36.7± 6.9	23.0
Halo		8	-39.7± 41.6	117.6	38.0± 11.1	31.3
H333+37	333/+37					
ThDi		40	-2.6± 6.0	37.7	28.4±2.1	13.0
MWTD		35	-2.7± 10.7	63.3	28.4± 3.7	21.8
Halo		20	36.5± 33.2	148.5	15.0±11.4	50.9
P741	339/+41					
ThDi		15	-49.1±10.9	42.3	50.1± 5.0	19.5
MWTD		17	-54.4±14.3	59.0	52.4± 6.5	26.9
Halo		2	-126.9± 29.0	41.0	86.1± 13.4	19.0
P802	339.5/+33					
ThDi		65	-32.1± 6.8	55.0	41.1± 2.9	23.3
MWTD		31	-14.4±11.1	61.6	33.6± 4.7	26.1
Halo		10	31.2± 41.0	129.7	14.2± 17.4	55.1

Table Fig10. Data for Figure 10

Distance Range kpc	Mean Distance kpc	N_{stars}	$\langle V_{LSR} \rangle$ km s ⁻¹	Std. Error ± km s ⁻¹
< 1.0	0.81	35	-10.7	7.8
1.0 – 1.5	1.30	132	-18.4	3.6
1.5 – 2.0	1.76	261	-15.7	3.0
2.0 – 2.5	2.23	279	-17.8	3.1
2.5 – 3.0	2.73	213	-20.1	3.7
3.0 – 3.5	3.23	155	-13.1	4.4
3.5 – 4.0	3.73	94	-18.3	5.5
4.0 – 4.5	4.21	48	-6.6	7.8
4.5 – 5.0	4.71	28	-4.3	12.0

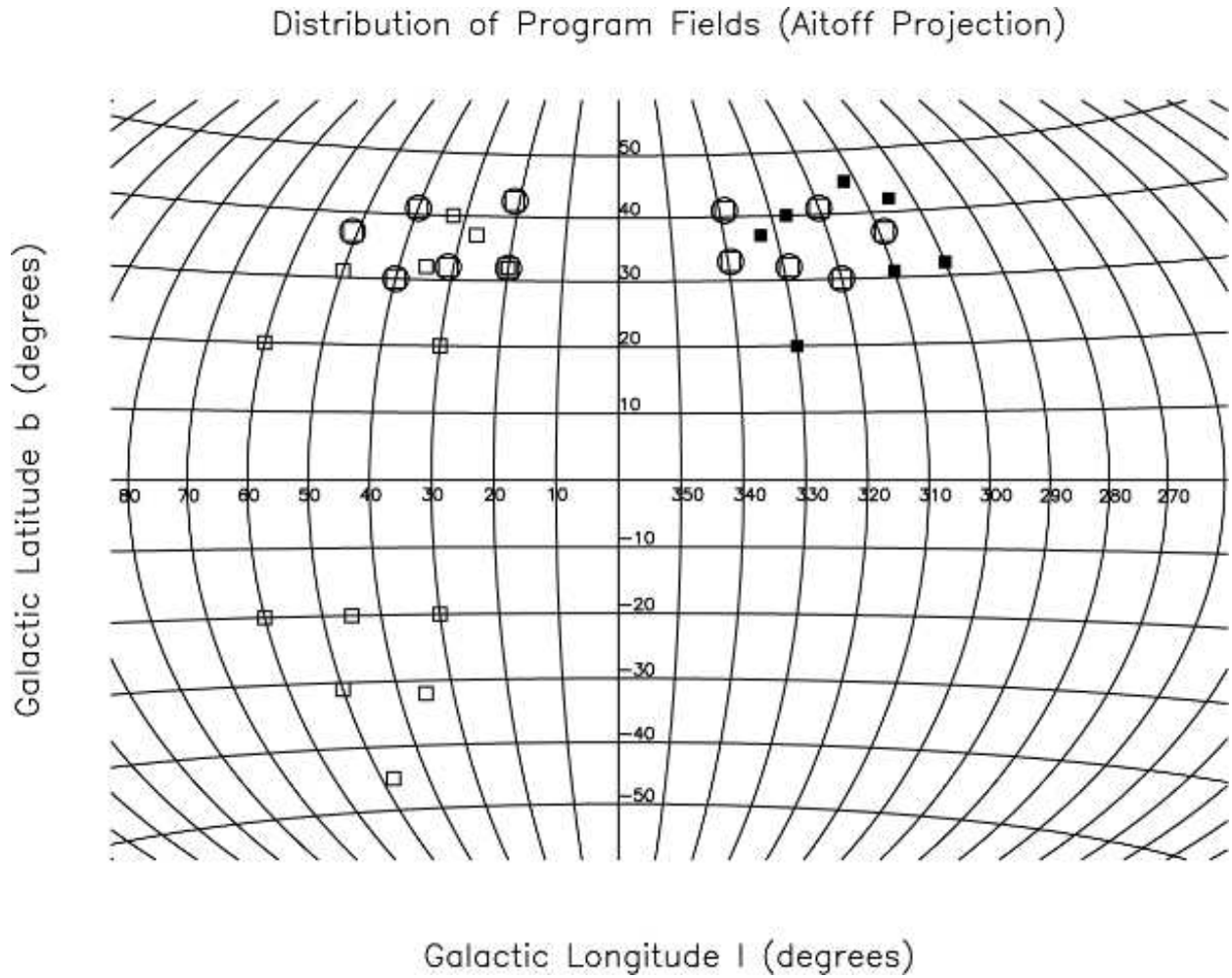


Fig. 1.— Distribution of the spectroscopy fields. Open squares were observed with the MMT/Hectospec, filled squares with CTIO/Hydra, and the circles are from Parker et al. (2004)

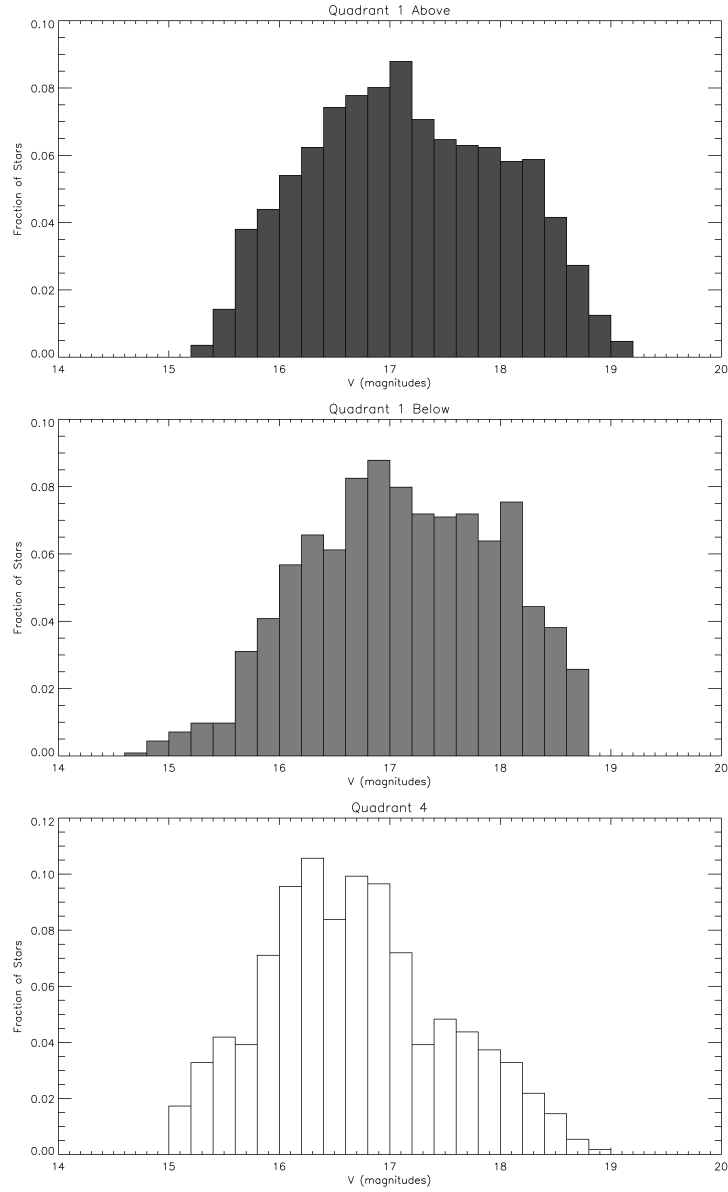


Fig. 2.— Histograms of V magnitudes.

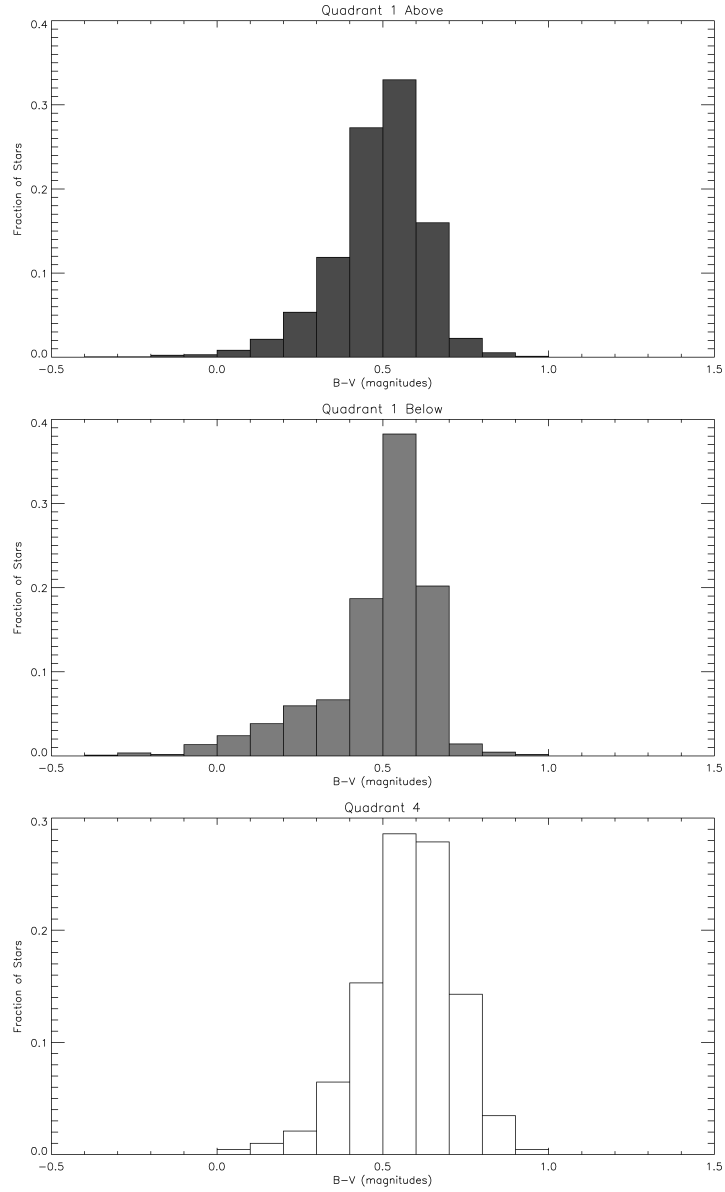


Fig. 3.— Histograms of $B - V$ corrected for interstellar extinction.

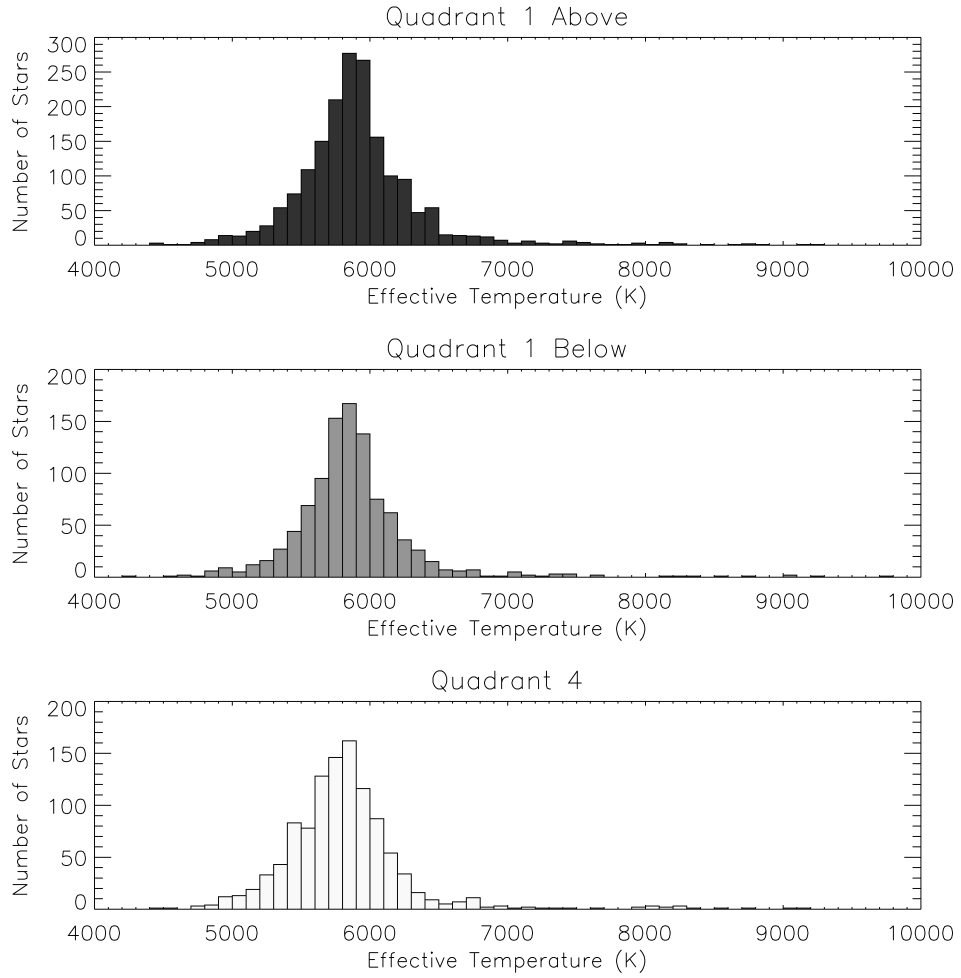


Fig. 4.— Histograms of effective temperature from the n-SSPP pipeline.

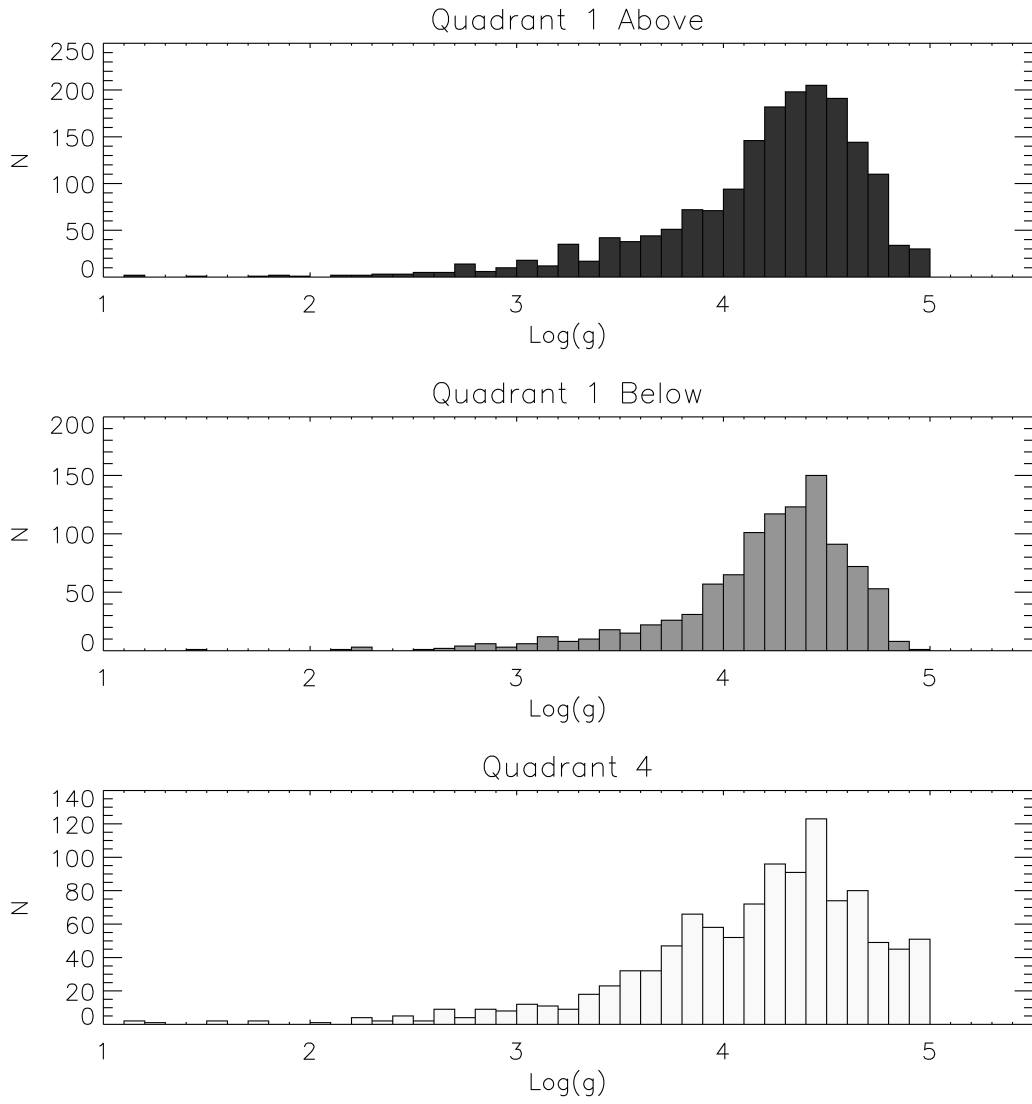


Fig. 5.— Histograms of $\log g$ (surface gravity) from the n-SSPP pipeline.

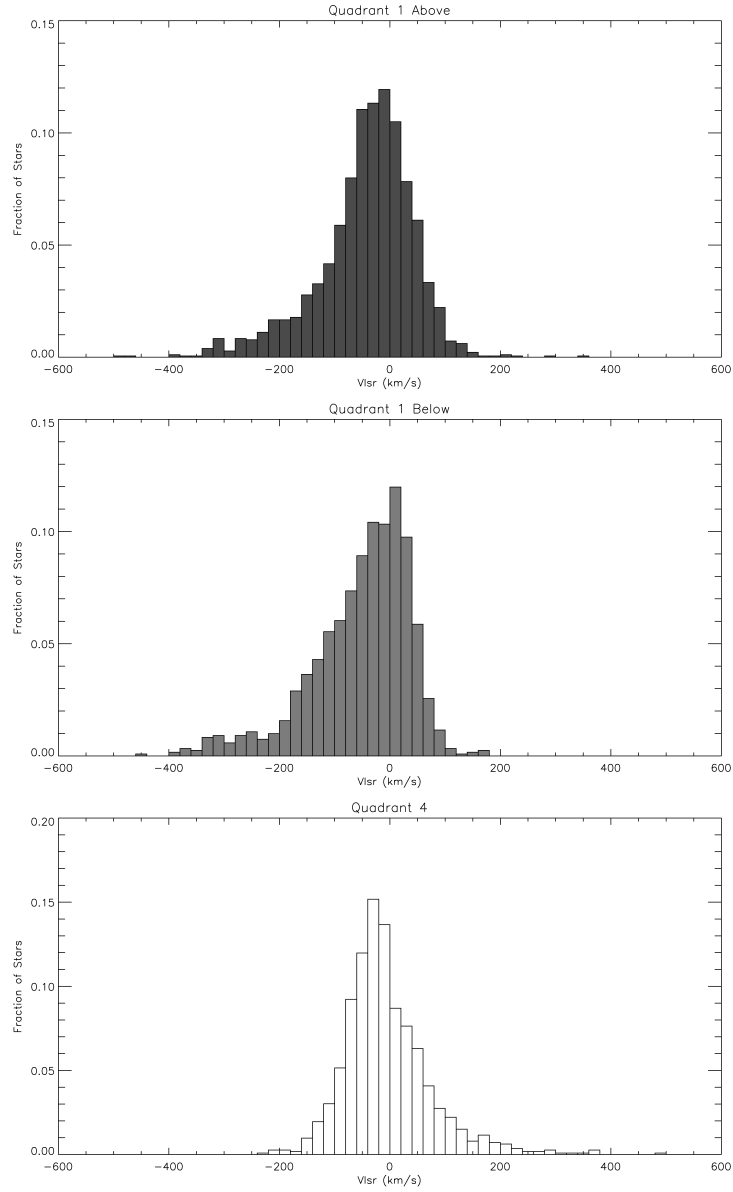


Fig. 6.— The normalized velocity distribution for V_{LSR} .

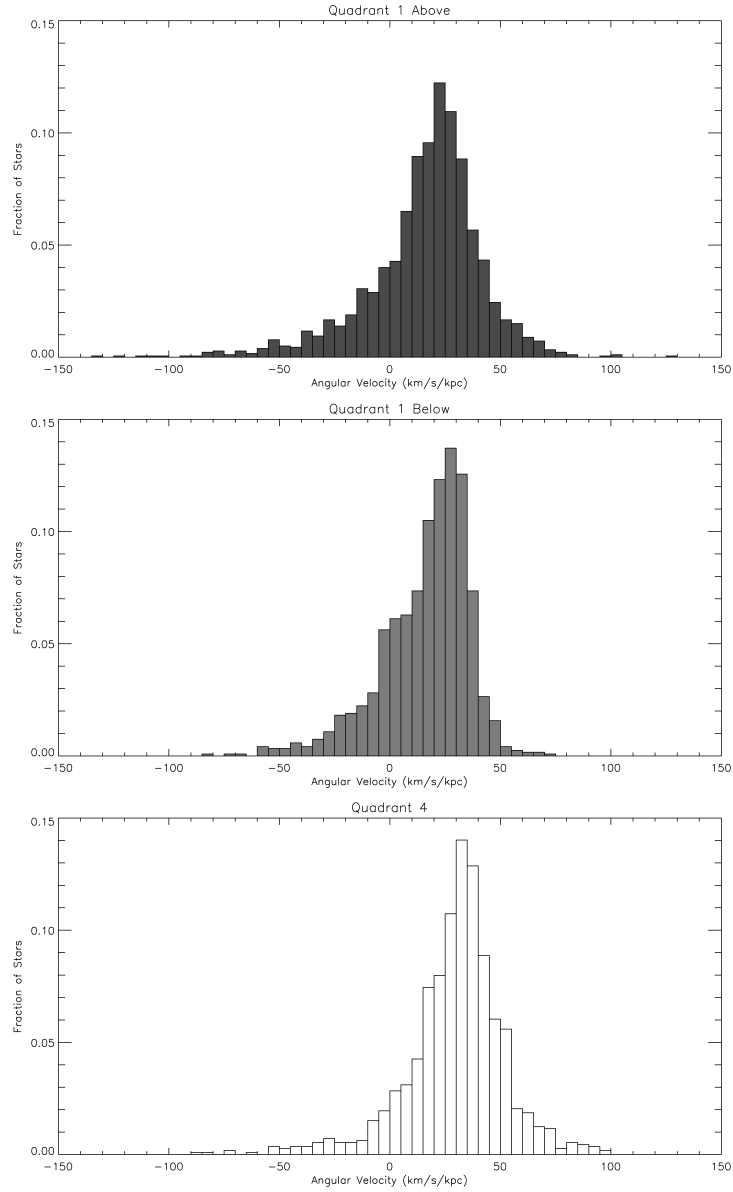
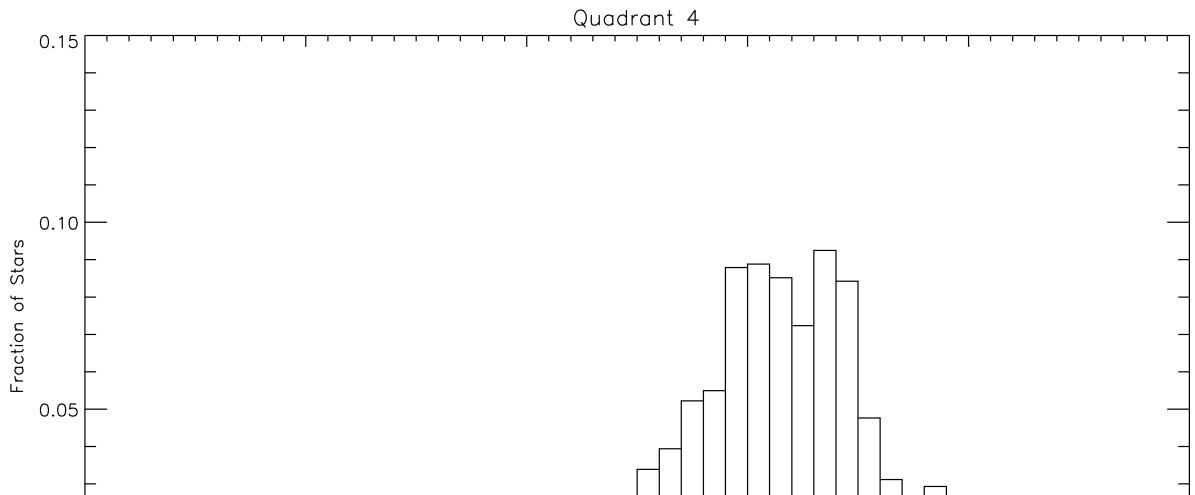
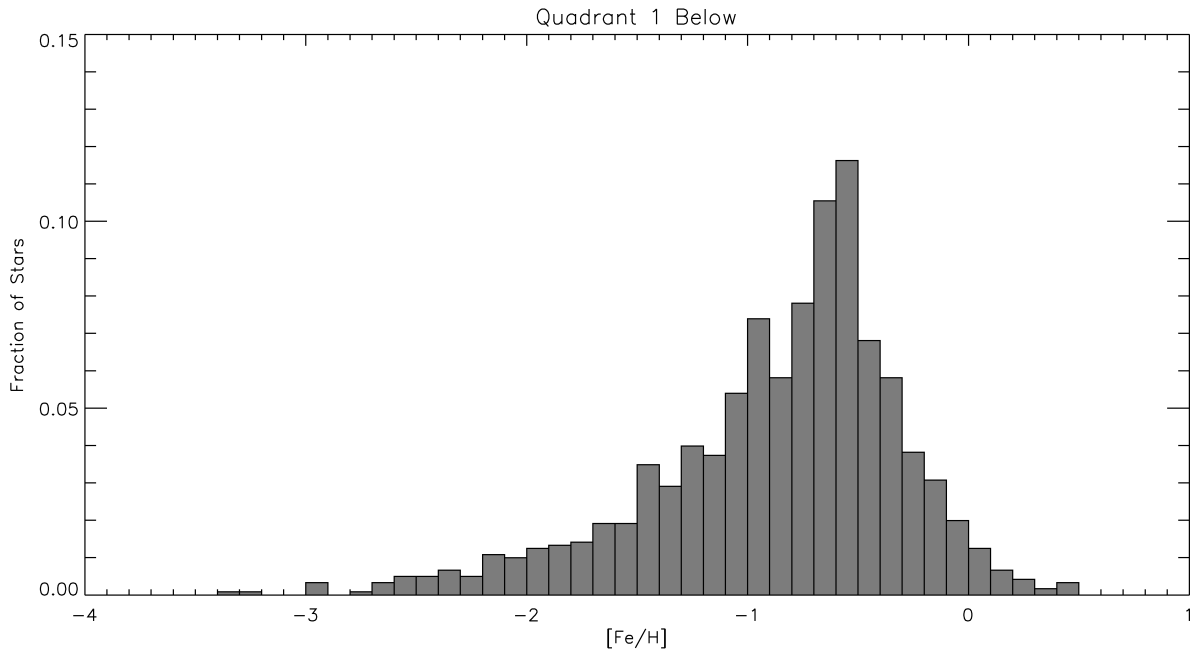
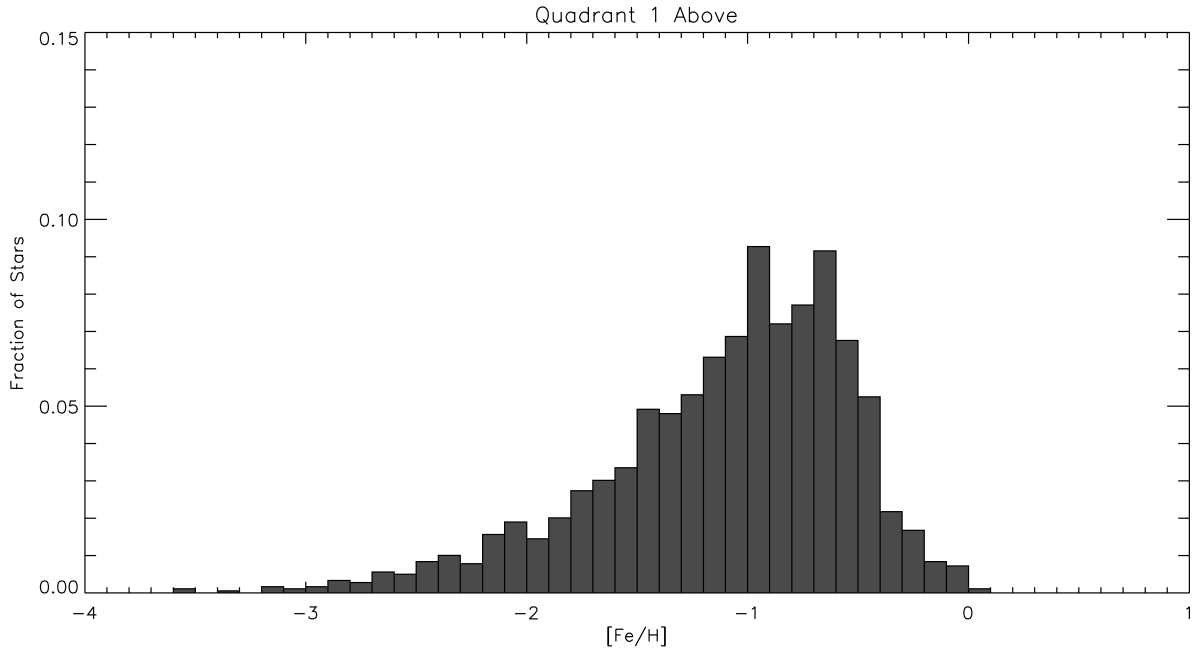


Fig. 7.— The normalized distribution for the rotation rate ω .



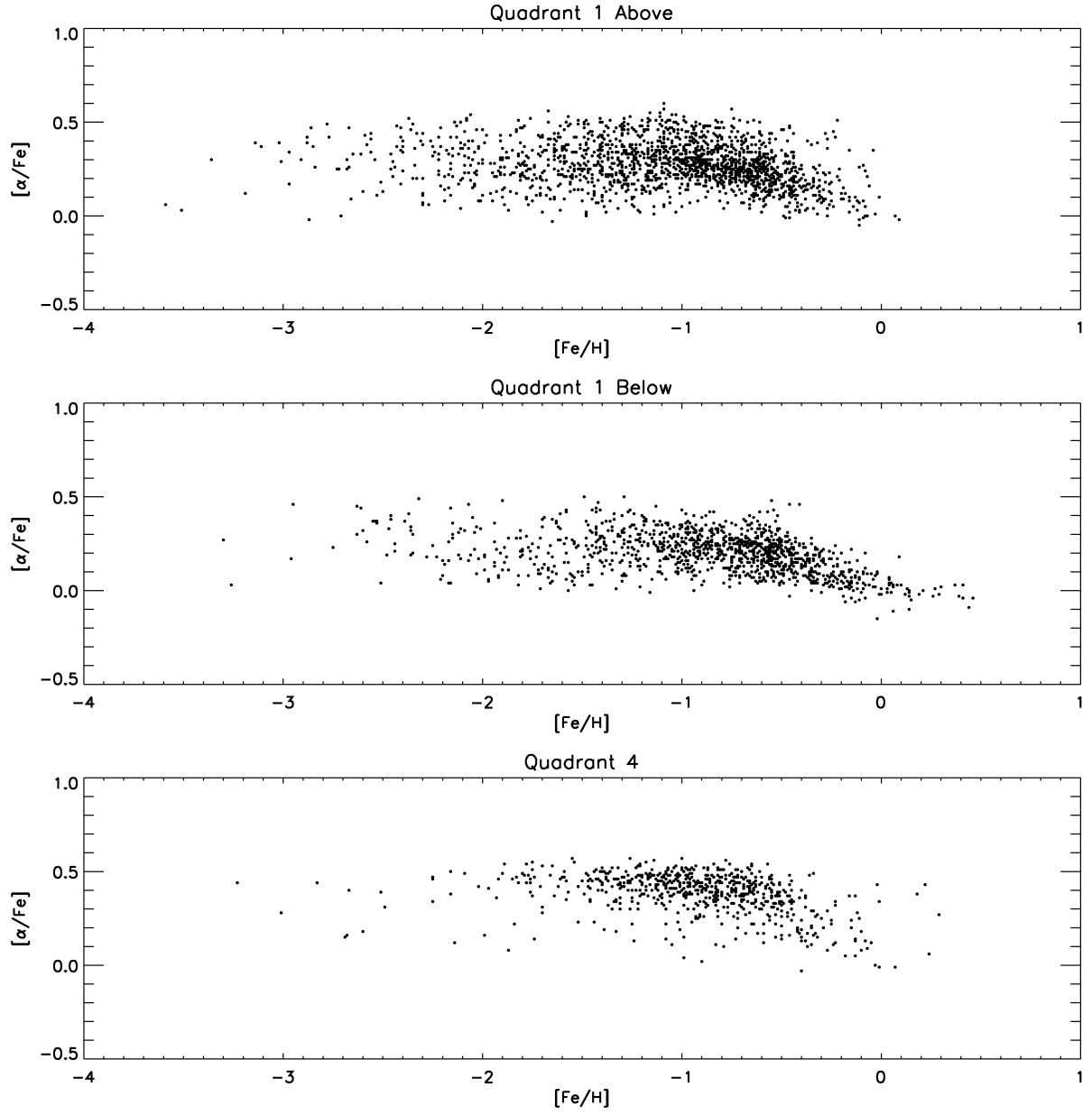


Fig. 9.— The $[\alpha/\text{Fe}]$ vs. $[\text{Fe}/\text{H}]$ diagrams for the three regions.

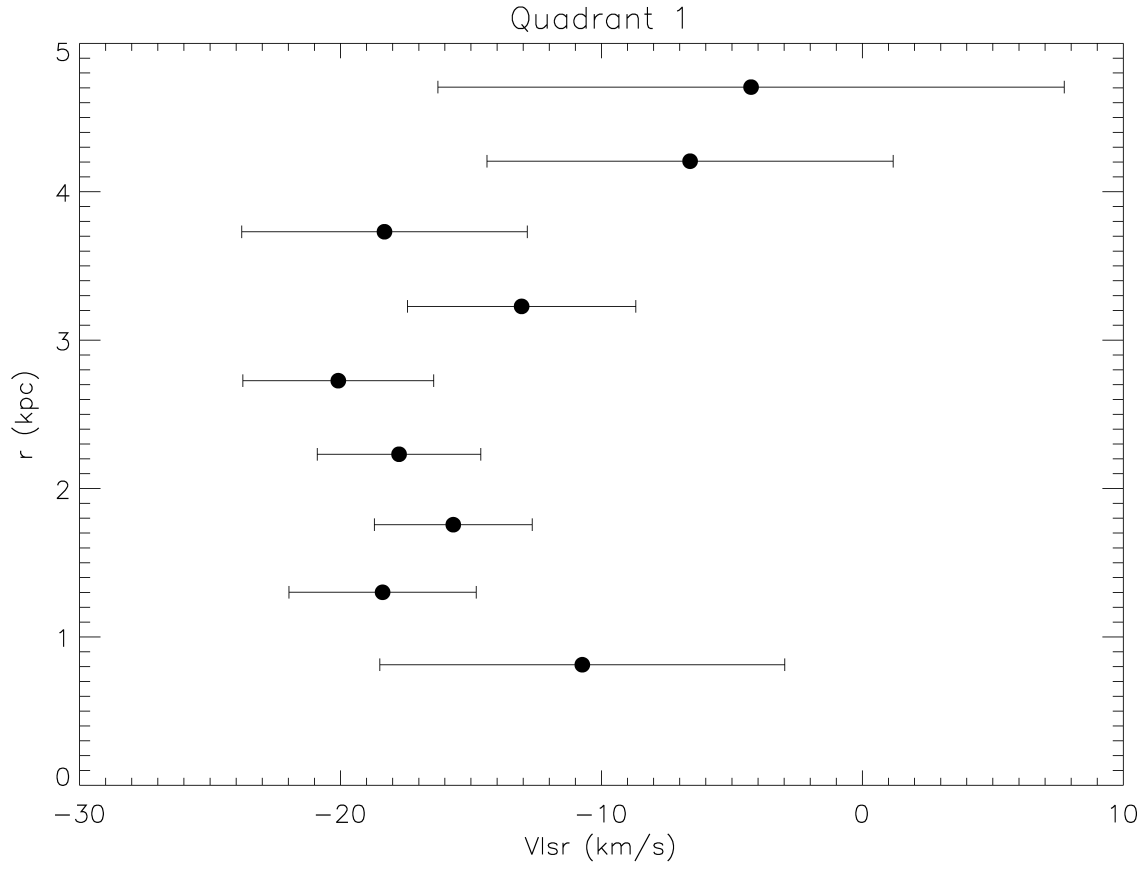


Fig. 10.— The mean V_{LSR} velocity as a function of distance from the Sun for the Thick Disk stars in in the first quadrant. Note the turnover or shift to less negative velocities at distances greater than 4 kpc.